JGR Atmospheres

RESEARCH ARTICLE
10.1029/2021JD034995

Key Points:

- Fluorine in the stratosphere is accumulating less rapidly in the Southern Hemisphere than in the Northern Hemisphere
- The observed fluorine trend asymmetry, attributed to transport circulation changes, opposes trends predicted by chemistry-climate models
- Observations and five modern reanalyses are qualitatively in agreement with these changes, calling for maintaining long-term observations

Supporting Information:

Supporting Information may be found in the online version of this article.

Correspondence to:

M. Prignon,
maxime.prignon@uliege.be

Citation:

Prignon, M., Chabrillat, S., Friedrich, M., Smale, D., Strahan, S. E., Bernath, P. F., et al. (2021). Stratospheric fluorine as a tracer of circulation changes: Comparison between infrared remote-sensing observations and simulations with five modern reanalyses. *Journal of Geophysical Research: Atmospheres*, *126*, e2021JD034995. https://doi.org/10.1029/2021JD034995

Received 31 MAR 2021
Accepted 7 SEP 2021

Stratospheric Fluorine as a Tracer of Circulation Changes: Comparison Between Infrared Remote-Sensing Observations and Simulations With Five Modern Reanalyses

M. Prignon[1], S. Chabrillat[2], M. Friedrich[3], D. Smale[4], S. E. Strahan[5,6], P. F. Bernath[7,8], M. P. Chipperfield[9,10], S. S. Dhomse[9,10], W. Feng[9,11], D. Minganti[2], C. Servais[12], and E. Mahieu[1]

[1]University of Liège, Institute of Astrophysics and Geophysics, UR SPHERES, Liège, Belgium, [2]Royal Belgian Institute for Space Aeronomy, Brussels, Belgium, [3]Department of Econometrics and Data Science, VU Amsterdam, Amsterdam, The Netherlands, [4]National Institute of Water and Atmospheric Research Ltd., Lauder, New Zealand, [5]Universities Space Research Association, Columbia, MD, USA, [6]NASA Goddard Space Flight Center, Greenbelt, MD, USA, [7]Department of Chemistry and Biochemistry, Old Dominion University, Norfolk, VA, USA, [8]Department of Chemistry, University of Waterloo, Waterloo, ON, Canada, [9]School of Earth and Environment, University of Leeds, Leeds, UK, [10]National Centre for Earth Observation, University of Leeds, Leeds, UK, [11]National Centre for Atmospheric Science, University of Leeds, Leeds, UK, [12]University of Liège, Institute of Astrophysics and Geophysics, STAR Institute, Liège, Belgium

Abstract Using multidecadal time series of ground-based and satellite Fourier transform infrared measurements of inorganic fluorine (i.e., total fluorine resident in stratospheric fluorine reservoirs), we investigate stratospheric circulation changes over the past 20 years. The representation of these changes in five modern reanalyses is further analyzed through chemical-transport model (CTM) simulations. From the observations but also from all reanalyses, we show that the inorganic fluorine is accumulating less rapidly in the Southern Hemisphere than in the Northern Hemisphere during the 21st century. Comparisons with a study evaluating the age-of-air of these reanalyses using the same CTM allow us to link this hemispheric asymmetry to changes in the Brewer-Dobson circulation (BDC), with the age-of-air of the Southern Hemisphere getting younger relative to that of the Northern Hemisphere. Large differences in simulated total columns and absolute trend values are, nevertheless, depicted between our simulations driven by the five reanalyses. Superimposed on this multidecadal change, we, furthermore, confirm a 5–7-year variability of the BDC that was first described in a recent study analyzing long-term time series of hydrogen chloride (HCl) and nitric acid (HNO_3). It is important to stress that our results, based on observations and meteorological reanalyses, are in contrast with the projections of chemistry-climate models in response to the coupled increase of greenhouse gases and decrease of ozone-depleting substances, calling for further investigations and the continuation of long-term observations.

Plain Language Summary The overturning circulation of the stratosphere is projected to change in response to increases in greenhouse gases and decreases in ozone-depleting substances, with the Southern Hemisphere branch expected to get weaker relative to the Northern Hemisphere. Here, we use 30-year time series of observations and simulations of a long-lived tracer to investigate stratospheric circulation changes. The observations analyzed are from ground-based and satellite instruments. We compare them with simulations that use a chemical-transport model driven by winds from meteorological reanalyses of 1990–2019. A reanalysis assimilates meteorological measurements into a forecast model to simulate the best possible representation of the atmospheric state. All five simulations, which use different reanalyses, agree with the observational analysis showing that the analyzed tracer is accumulating less rapidly in the Southern Hemisphere than in the Northern Hemisphere through 2019. This hemispheric asymmetry is attributed to changes in the stratospheric transport circulation, with the Southern Hemisphere branch getting stronger relative to the Northern Hemisphere. Our results support the conclusions of a recent observational study but do not support circulation changes projected by chemistry-climate models. This study highlights the crucial importance of long-term observation time series.

1. Introduction

The spatial distribution of long-lived constituents in the stratosphere is directly related to the Brewer-Dobson circulation (BDC) and its changes (Plumb, 2007). Depending on the theoretical model considered, the BDC can either refer strictly to the stratospheric overturning residual circulation or may also include a two-way irreversible mixing (see Butchart, 2014, for a complete review of BDC models). In this study, both the effects of advection and mixing are considered when referring to the BDC. Using this definition, the BDC corresponds to the net transport of tracers occurring in the stratosphere. Emissions of greenhouse gases and ozone-depleting substances (ODS) are expected to strongly affect the BDC through radiative and dynamical coupled effects. The increase of greenhouse gases causes a radiative heating (cooling) of the troposphere (stratosphere), modifying the wave activity that drives the BDC. As a consequence, chemistry-climate models (CCMs) have robustly projected a speeding up of the BDC (e.g., Butchart, 2014, and references therein). On the other hand, ODS have been strongly depleting the ozone layer in the 20th century, particularly above the Antarctic with the formation of the ozone hole (WMO, 2018). Again, the resulting radiative temperature change is believed to affect the dynamics of the BDC. Recent studies, accounting this time for the forcing of both the greenhouse gases and ODS, have shown that the latter have contributed about half of the BDC acceleration in the 20th century (e.g., Abalos et al., 2019; Polvani et al., 2017, 2018, 2019). With the success of the Montreal Protocol on Substances that Deplete the Ozone Layer, ODS have been decreasing and ozone recovery is expected to occur during the 21st century. CCMs project an opposite response of the BDC to the decrease of ODS relative to that of the increase of greenhouse gases, that is a reduced BDC in the Southern Hemisphere due to the ozone hole recovery (Polvani et al., 2019). The global forcing of ODS, projected by CCMs for the 21st century, reduces the greenhouse-gas-induced speeding up of the BDC by a factor of 2 but the degree of cancellation between the two forcings will vary as a function of the true evolution of ODS and greenhouse gases compared to the considered forcing scenarios (Polvani et al., 2019).

Confirming these model results is challenging as no direct observations of the BDC and its trends are available. Time series of air temperature or long-lived tracers can, however, be used as proxies of the BDC. Very long-lived species increasing monotonically at the surface (e.g., CO_2 or SF_6) can, moreover, be used to derive the age-of-air (AoA). AoA is a direct diagnostic of the BDC as it is defined as the transit time from either, depending on the definition used, the Earth's surface or entrance in the stratosphere, to a particular location in the stratosphere (Waugh & Hall, 2002). From satellite temperature observations and eddy heat fluxes from the European Centre for Medium-Range Weather Forecasts Interim reanalysis (ERA-Interim; Dee et al., 2011), Fu et al. (2019) determined that the mean BDC has accelerated over 1980–2018. Moreover, they also determined that the BDC has accelerated for the period 1980–1999 and has decelerated for the period 2000–2018, which are periods of ozone depletion and recovery, respectively. Fu et al. (2019) also evaluated the hemispheric contribution and showed that, for both periods, most of the change was coming from the Southern Hemisphere, although the trends were not significant at the 90% confidence level. AoA trends derived from balloon-borne observations (Engel et al., 2009, 2017) provided inconclusive results with a positive but not significant AoA trend in the Northern Hemisphere midlatitudes for the period 1975–2016 (Engel et al., 2017). Despite the fact that this time series is relatively long, it is only based on around 30 CO_2 and SF_6 vertical profiles between altitudes of 24–35 km (including a gap of 10 years between 2005 and 2015). Therefore, the sparse and irregular sampling may have hindered any trend detection (Garcia et al., 2011). Recently, Fritsch et al. (2020) also demonstrated the sensitivity of mean AoA trends derived from SF_6 balloon-borne observations to the derivation methods and their parameters. Choosing new parameter values in agreement with a model simulation, they further computed closer to zero trend values for the mean AoA time-series derived from the SF_6 balloon-borne observations. AoA global trends (2002–2012) were also estimated from SF_6 global measurements performed by the Michelson Interferometer for Passive Atmospheric Sounding (MIPAS) satellite instrument (Haenel et al., 2015; Stiller et al., 2012) and showed opposite values for the two hemispheres, with positive values in the Northern Hemisphere (in agreement with Engel et al., 2009) and negative values in the Southern Hemisphere.

Several long-lived tracer time series have now been successfully exploited to track BDC changes, for example, hydrogen chloride (HCl; Mahieu et al., 2014), nitrous oxide (N_2O; Nedoluha et al., 2015; Stiller et al., 2017), ozone (Nedoluha et al., 2015), hydrogen fluoride (HF; Harrison et al., 2016), HCFC-22 ($CHClF_2$; Chirkov et al., 2016), and carbonyl sulfide (OCS; Glatthor et al., 2017). Mahieu et al. (2014) noted an unexpected HCl

increase in time series of ground-based Fourier transform infrared (FTIR) spectrometers and satellite measurements as well as of a chemical-transport model (CTM) driven by ERA-Interim, occurring only in the Northern Hemisphere in 2007–2011. They attributed this increase to circulation changes, that is, to a deceleration of the BDC in the Northern Hemisphere, as a CTM simulation with perpetually repeating dynamics did not show any positive trend in the time series. Later on, Stiller et al. (2017) also reported a hemispheric asymmetry in N_2O and AoA trends computed from satellite and CTM (driven again by ERA-Interim) data. They further analyzed BDC diagnostics, that is, the position of the subtropical transport barriers (derived from observations and model outputs), the turnaround latitude, and the latitude of the meridional trace gas gradient genesis (from ERA-Interim), to conclude that a southward shift by about 5° of the tropical transport barriers could explain the observed and modeled hemispheric asymmetry in trends. Recently, Strahan et al. (2020) reported on hemispheric asymmetry in trends of long-lived tracers and AoA through an analysis of longer (1994–2018) NDACC (Network for the Detection of Atmospheric Composition Change; De Mazière et al., 2018; http://www.ndacc.org) FTIR time series of HCl and nitric acid (HNO_3). These results place the previously reported trends in a longer context where interhemispheric anomalies of long-lived tracers and AoA exhibit a 5–7-year period. The reported hemispheric asymmetry in 2005–2012 in Mahieu et al. (2014; HCl) and Stiller et al. (2017; N_2O and AoA) is, for example, located between a large positive interhemispheric anomaly (peaking around 2005) and a large negative one (peaking around 2011; Southern Hemisphere minus Northern Hemisphere). Finally, Strahan et al. (2020) also indirectly derived AoA trends from NDACC FTIR HCl and HNO_3 interhemispheric anomalies using a CTM AoA simulation driven by MERRA-2 (National Aeronautics and Space Administration's Modern Era Retrospective-analysis for Research Applications version 2; Gelaro et al., 2017). They concluded that the Southern Hemisphere AoA is getting younger by 1 month per decade compared to that of the Northern Hemisphere for the period 1994–2018. This decreasing AoA trend could correspond to an acceleration of the BDC in the Southern Hemisphere, which would be in contrast with the projections of CCMs (Polvani et al., 2019) and the stratospheric temperature study of Fu et al. (2019).

At present, there is no clear consensus on what causes the observed and modeled hemispheric asymmetries. While Stiller et al. (2017) showed that a 5° southward shift of the tropical transport barriers could be the cause, Strahan et al. (2020) attributed the hemispheric asymmetries to a variability in the BDC driven by an interaction between the BDC annual cycle and the quasi-biennial oscillation (QBO). This multiyear variability was previously described by Ploeger and Birner (2016) to explain AoA spectrum anomalies in the midlatitude lower stratosphere and may also explain the N_2O and HCl anomalies highlighted in previous works of Strahan et al. (2014, 2015). Assessing the respective contribution of residual circulation and mixing has also led to conflicting results. Han et al. (2019) found that eddy mixing has a negligible impact on circulation changes compared to the residual circulation (dynamical transport) and furthermore stated that the southward shift of the upwelling region only partly explains the hemispheric asymmetry. In contrast, Ploeger et al. (2015) showed that AoA changes (2002–2012) are the result of combined effects of residual circulation and mixing, the latter having a stronger effect in the lower stratosphere.

While meteorological reanalyses provide a way to quantify and characterize changes in circulation and mixing, the substantial differences in age spectra and mean ages among the reanalyses lead to significant uncertainty in their trends. The SPARC (Stratosphere-troposphere Processes And their Role in Climate) Reanalysis Intercomparison Project (S-RIP) aims at a better understanding of these differences to eventually improve the compared reanalyses. Fujiwara et al. (2017) provide an overview of the reanalyses included in the SPARC S-RIP project comparing, for example, assimilated data sources, forecast models, or spatial grids. Recently, Chabrillat et al. (2018) and Ploeger et al. (2019) have compared AoA retrieved from the main modern reanalyses then available, that is, ERA-Interim (Dee et al., 2011), the Japanese Meteorological Agency's Japanese 55-year Reanalysis (JRA-55; Kobayashi et al., 2015), MERRA (Rienecker et al., 2011; not included in Ploeger et al., 2019), and MERRA-2 (Gelaro et al., 2017). Both studies highlighted large differences in mean AoA and full age spectrum (only evaluated in Ploeger et al., 2019). MERRA and MERRA-2 are the reanalyses with the oldest AoA, JRA-55 the youngest, with ERA-Interim in between but closer to JRA-55. Whereas discrepancies are found between both studies for decadal trends, ERA-Interim is the only reanalysis to show a hemispheric asymmetry (or dipole structure) in AoA trends in both studies for the period 2002–2015, with positive values in the Northern Hemisphere and negative ones in the Southern Hemisphere. Differences in decadal trends between the studies of Chabrillat et al. (2018) and Ploeger et al. (2019)

are attributed to the different types of transport model used, that is, a kinematic model only driven by the surface pressure and horizontal wind fields in Chabrillat et al. (2018) and a diabatic model driven also by the heating rates of reanalyses in Ploeger et al. (2019).

A better characterization of the BDC and its interannual variability is crucial as it strongly influences ozone trend assessments. To scrutinize the onset of the ozone recovery and thus the success of the Montreal Protocol, reducing the uncertainty around the trend values of ozone is, in fact, a key requirement (SPARC/IO3C/GAW, 2019; WMO, 2018). Additionally, most of CCMs, employed for climate projections, still fail to correctly reproduce the observed midlatitude lower stratosphere trend of ozone due to enhanced mixing of tropical air into the midlatitudes (Ball et al., 2020). As concluded recently by Strahan et al. (2020), the disagreements between, on the one hand, observations and reanalyses and, on the other hand, CCMs, require additional studies assessing long-term trends from observational data sets as long-lived tracers. Finally, the BDC and its changes are also key drivers of variability observed in the tropospheric circulation and composition as highlighted in recent studies (e.g., Banerjee et al., 2020; Ray et al., 2020).

In this study, we investigate multidecadal trends of the BDC as well as its interannual variability most recently described in Strahan et al. (2020). Here, we make use of time series of total inorganic fluorine (F_y) as retrieved from ground-based Fourier-transform infrared (FTIR) measurements as well as FTIR satellite observations (Sections 3.1 and 3.2). Outside the context of the BDC trends and multiyear variability, assessing long-term trends of inorganic fluorine is also of great interest in the framework of the Montreal Protocol as HFCs (not chlorinated but having large global warming potentials) are now also regulated through the recent Kigali Amendment to the Protocol (entered into force on January 1, 2019). In the framework of the SPARC S-RIP project, we also include long-term simulations performed by the BASCOE CTM (Section 3.3.1) driven by the main modern reanalyses, that is, ERA-Interim, JRA-55, MERRA, MERRA-2, as well as the new ECMWF reanalysis, ERA5 (Hersbach et al., 2020).

Section 2 provides a brief theoretical introduction to the F_y budget. Section 3 describes the data sets and methods employed in this research. Section 4.1 describes the observed and simulated F_y budget above Jungfraujoch (46°N) and Lauder (45°S) NDACC stations and discusses on the marginal contribution of COClF to F_y. Section 4.2 presents and describes the inorganic fluorine time series used for the trend analyses of Section 5. These results are discussed in Section 6 in the context of recent studies and Section 7 draws the main conclusions and outcomes of this work.

2. Fluorine in the Stratosphere

Fluorine in the stratosphere originates from the photochemical destruction of anthropogenic CFCs, hydrochlorofluorocarbons (HCFCs), and hydrofluorocarbons (HFCs; e.g., Harrison et al., 2016). The most abundant CFCs, HCFCs, or HFCs (see hereafter) have long atmospheric lifetimes ranging from 10 to 100 years, although some HFCs may be short-lived with lifetimes of several days only. Consequently, these source gases largely reach the stratosphere where they undergo photolysis and oxidation by $O(^1D)$ or OH (HCFCs and HFCs) to form inorganic reservoirs. In atmospheric chemistry, organic fluorine refers to the fluorinated tropospheric source gases while inorganic fluorine refers to the chemical species resulting from the decomposition of these species. Figure 1 shows the increase of CFCs until the 1990s, followed by their gradual decrease and gradual replacement by HCFCs and HFCs. The global mixing ratios given in Figure 1 were derived from in situ measurements and were compiled for the Coupled Model Intercomparison Project Phase 6 (CMIP6; Meinshausen et al., 2017, 2020). Due to their very long lifetimes, CFCs are still the most abundant halocarbons, with CFC-12 (CCl_2F_2; 516.1 ppt), CFC-11 (CCl_3F; 229.6 ppt), and CFC-113 (CCl_2FCClF_2; 71.4 ppt) the top three most-abundant CFCs in 2016 (the numerical values are the global volume mixing ratios at surface as given in WMO, 2018). HCFC-22 ($CHClF_2$) is by far the most abundant HCFC with a global mole fraction of 237.4 ppt in 2016 (WMO, 2018). CFC production and consumption are currently banned and HCFC consumption and production are banned in developed countries and are strongly regulated in developing countries by the Montreal Protocol (and its later adjustments). Consequently, the planned transition to HFCs has led to a rapid increase of HFC-134a (CH_2FCF_3), with its global mixing ratio reaching nearly 90 ppt in 2016 while being close to 0 in 1995 (WMO, 2018). It should be noted that the total abundance of fluorine at the surface increased almost linearly between 1993 and 2014 (Figure 1).

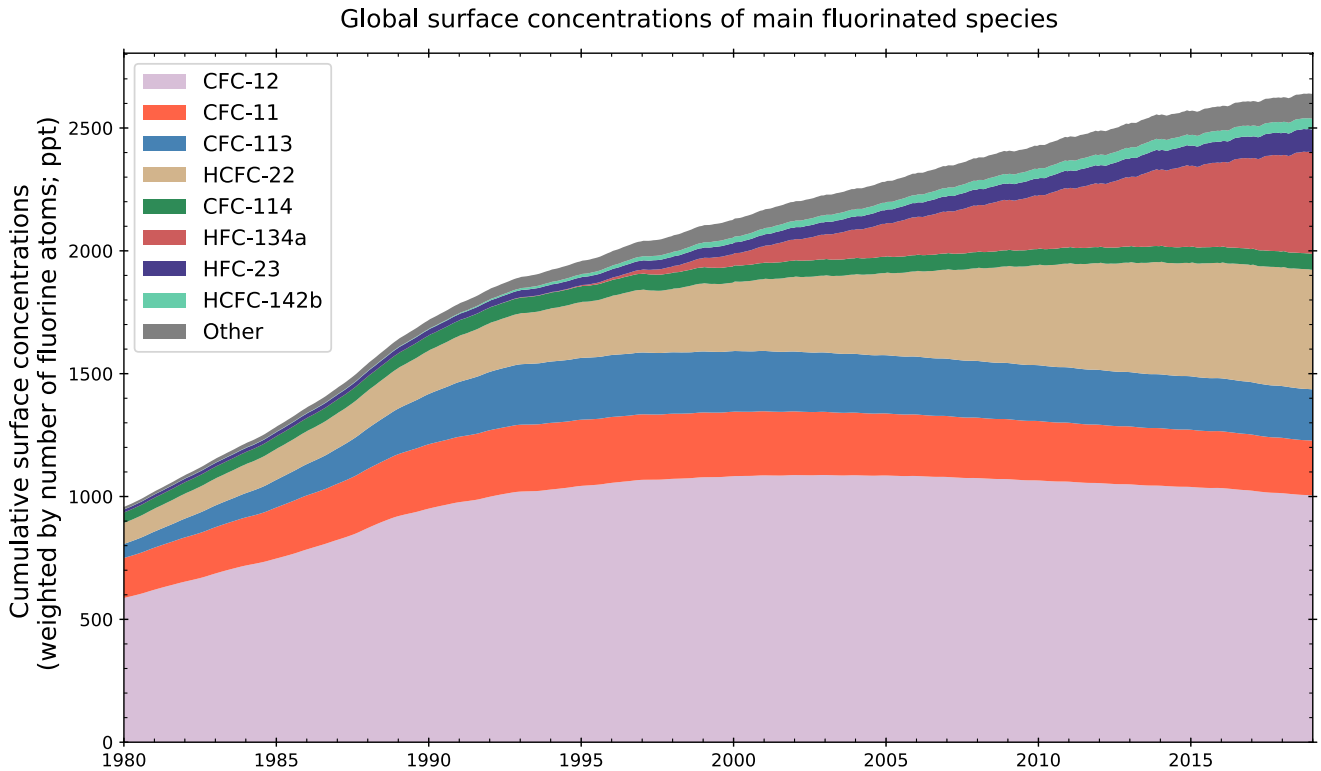

Figure 1. Global means of the surface volume mixing ratios of the main fluorinated species as given in Meinshausen et al. (2017, 2020; see Section 3.3.1). Mixing ratios are weighted by the number of fluorine atoms in each species (e.g., 2 × [CFC-12]). "Other" contributions (gray) comprise the species CFC-115, HCFC-141b, HFC-152a, Halon-1211, and Halon-1301.

For the major halocarbons, species with at least two fluorine atoms (i.e., CFC-12, HCFC-22, and HFC-134a) follow a reaction path leading to the formation of COF_2, while CFC-11, containing a single fluorine atom, follows another reaction path leading to the formation of COClF (Harrison et al., 2016). CFC-113 follows similar paths but degrades into both COClF and COF_2. These two fluorine reservoirs in turn undergo photolysis to release fluorine atoms, which quickly react with methane, water, or molecular hydrogen to form the ultimate, and very stable, fluorine reservoir, HF. With less abundant sources and a weaker stability, COClF is by far the least abundant inorganic fluorine reservoir and is decreasing in the atmosphere in line with its major sources (e.g., Bernath et al., 2020). Conversely, COF_2 is increasing because the positive trends in both HCFC-22 and HFC-134a more than compensate for the decreasing abundances of CFC-12 and CFC-113 (e.g., Bernath et al., 2020; Harrison et al., 2014). Finally, HF has no major chemical sink in the stratosphere and is slowly removed by transport (into both the troposphere and the mesosphere) and by rainout. Consequently, HF is still increasing in the atmosphere (i.e., 0.5% in 2004–2012) although less rapidly than before (i.e., 5% in 1991–1997; Harrison et al., 2016; WMO, 2018).

The total inorganic fluorine (F_y) is defined as the sum, weighted by the number of fluorine atoms, of either volume mixing ratios or total columns of HF, COF_2, and COClF:

$$\left[F_y\right] = \left[HF\right] + 2\left[COF_2\right] + \left[COClF\right]. \quad (1)$$

Due to the unavailability of COClF in the FTIR retrievals (see Section 3.1), we also define a budget of inorganic fluorine that excludes this reservoir:

$$\left[{}^{*}F_y\right] = \left[HF\right] + 2\left[COF_2\right]. \quad (2)$$

As the total inorganic fluorine is produced by the photolysis of halocarbons, minimum volume mixing ratios are encountered in the lower tropical stratosphere. Following the deep branch of the BDC and ascending in the tropical stratosphere, the availability of high-energy ultraviolet photons increases and photolysis becomes more efficient, and the total inorganic volume mixing ratios become larger. The downwelling

branches of the circulation transport air that is rich in F_y into the extratropical latitudes of the lower stratosphere.

3. Data and Methods

3.1. Ground-Based FTIR Retrievals

This study relies on time series from the Jungfraujoch (Switzerland, 46.55°N) and Lauder (New Zealand, 45.04°S) NDACC stations. Jungfraujoch and Lauder stations generated multidecadal and regular records of high-resolution (0.003–0.006 cm^{-1}) FTIR solar absorption spectra recorded under clear-sky conditions. Since the most striking BDC changes have been observed through differences between the northern and southern midlatitudes (see Section 1), these two stations are particularly suited for such investigations.

While HF is retrieved at most of the NDACC stations, COF_2 is a more challenging species to retrieve from ground-based FTIR spectra due to very weak absorption lines. The only published COF_2 retrieval methods from ground-based infrared solar spectra are in Melen et al. (1998) and Duchatelet et al. (2009) and were only applied to the Jungfraujoch observations. Here, this strategy was applied to Lauder spectra as well. COClF is, to our knowledge, currently not retrieved at any FTIR NDACC sites due to its very weak features blinded by water vapor strong interferences. Therefore, the inorganic budget as retrieved from ground-based FTIR ($*F_y$; see Equation 2) is not totally closed. Nassar et al. (2006) showed that the contribution of COClF to the total inorganic fluorine abundance is very small compared to HF and COF_2 hence the ground-based FTIR $*F_y$ should be a very good approximation to F_y. This approximation will be further investigated in Section 4.1.

We apply the optimal estimation method developed by Rodgers (2000), implemented in the SFIT-4 v.0.9.4.4 algorithm, to perform the retrievals of HF and COF_2 total columns (mol./cm^{-2}; integrated from the station altitude to the top of the atmosphere) from the solar infrared spectra. At Jungfraujoch, spectra were recorded by a homemade instrument from 1984 to 2008 and have been recorded by a Bruker IFS 120HR spectrometer from the early 1990s to present (see Zander et al., 2008). At Lauder the spectrometers are a Bruker IFS 120M (1996–2002), a Bruker IFS 120HR (2002–2018), and a Bruker 125HR (2018 to present; Kohlhepp et al., 2012; Strahan et al., 2020).

3.1.1. HF

HF retrievals from the Jungfraujoch spectra are performed following the retrieval strategy described in Duchatelet et al. (2010). The microwindow considered is from 4,038.80 to 4,039.11 cm^{-1} and includes water vapor (H_2O) and methane (CH_4) as interfering species (i.e., their vertical distributions are scaled during the spectrum inversion). A signal-to-noise ratio of 500 is assumed in all inversions, for both instruments. Diagonal elements of the a priori covariance matrix are set to 70% km^{-1} along with a Gaussian interlayer correlation of 3 km at half-width. The total systematic error is estimated to be around 5.5% while the random error is estimated to be around 2% (estimated using the formalism of Rodgers, 2000).

For Lauder, a second microwindow is included for the spectrum inversion (4,109.77 –4110.07 cm^{-1}) to better adjust the interfering species (Kohlhepp et al., 2012). Fixed signal-to-noise ratios of 230, 270, and 320 are assumed for the Bruker IFS 120M, the Bruker IFS 120HR, and the Bruker 125HR, respectively. Diagonal elements of the a priori covariance matrix are set to 50% km^{-1} along with a Gaussian interlayer correlation of 4 km at half-width. The total systematic error is estimated to be around 2.5% while the random error is estimated to be around 1.25%.

For both sites, the mean vertical profile of HF computed from a WACCM version 4 (Whole Atmosphere Community Climate Model) 40-year run (1980–2020) is used as the a priori profile for the inversion. Line-by-line spectroscopic parameters are taken from HITRAN 2008 (Rothman et al., 2009).

3.1.2. COF_2

To retrieve enough information despite the very weak absorption lines of COF_2 in the infrared spectral region, Duchatelet et al. (2009) proposed a multi-spectrum fitting approach. In this strategy, the microwindows taken from different spectra recorded during the same day or half-day are fitted simultaneously by the

retrieval process. This way, the combined spectra allow the inverse method to retrieve more information from the measurement (i.e., lower dependence from the a priori, see Table 2 in Duchatelet et al., 2009).

For Jungfraujoch, we apply the multi-spectrum approach developed for the spectra recorded at the station. The strategy allows to retrieve COF_2 columns from spectra recorded by the two detectors of the Bruker instrument (MCT and InSb) as well as the InSb detector of the homemade FTS. We include the same microwindows as in Duchatelet et al. (2009). As Melen et al. (1998), we note a systematic difference of around 6% between the total columns retrieved from spectra recorded by the InSb and the MCT detectors (MCT columns being higher). As there is no trend in the systematic differences, we applied a simple constant scaling factor (computed over daily mean coincidences) to scale the MCT time series toward that of the InSb, thus avoiding the scaling of the homemade instrument time series. We assume a fixed signal-to-noise ratio of 250 for the retrievals of COF_2.

COF_2 retrievals at Lauder are performed using a different approach. Rather than fitting simultaneously several spectra, the strategy applied at Lauder is based on co-adding all spectra within a month over a defined solar zenith angle range (70–80°) to increase the signal-to-noise ratio. The combination of spectra is performed using the approach outlined in Notholt and Lehmann (2003). Consequently, FTIR COF_2 retrievals from Lauder have a monthly sampling. At Lauder, only the spectra recorded by the MCT detectors are used to retrieve COF_2. The co-adding of spectra allows to approximately double the signal-to-noise ratio, thus a fixed signal-to-noise ratio of 400 is assumed for Lauder COF_2 retrievals.

For both stations, we have updated the a priori profile of COF_2 using measurements of the Atmospheric Chemistry Experiment Fourier Transform Spectrometer (ACE-FTS, see Section 3.2) performed between 2004 and 2019. The a priori profile is completed with WACCM v4 outputs below 15 km. For Jungfraujoch (Lauder) we make use of ACE-FTS measurements included between 40° and 50°N (40° and 50°S). For the a priori covariance matrix, we follow Duchatelet et al. (2009) and set the diagonal elements of the a priori covariance matrix to 60% km^{-1} along with a Gaussian interlayer correlation of 2 km at half-width. As for HF, line-by-line spectroscopic parameters are taken from the HITRAN 2008 compilation.

Systematic errors are estimated to be relatively high for COF_2 retrievals as a large uncertainty of the spectroscopic parameters is assumed (15%–20%) while the total random error is estimated to be around 10% (see also Duchatelet et al., 2009).

3.1.3. Error Budget for $*F_y$

The retrieval errors for HF and COF_2 total columns, as assessed using the method of Rodgers (2000), may be combined to estimate the net error for $*F_y$ total columns. To do so, we multiply the COF_2 absolute errors for total columns by 2 (for the two fluorine atoms) and add it to the HF total column errors. Relative errors are then obtained by dividing the absolute errors by the $*F_y$ total columns (e.g., Zander et al., 1992). Following this method, we assess that the systematic error for $*F_y$ total columns is around 10% and that the random error is around 5%. Combining these two errors in quadrature, we assess the total error for $*F_y$ total columns to be around 11%.

3.2. ACE-FTS

Observations from the Atmospheric Chemistry Experiment Fourier Transform Spectrometer (ACE-FTS) on board the SCISAT satellite are also included in this work (Bernath et al., 2005; Bernath, 2017). Besides their involvement in the cross-validation between ground-based and satellite FTIR observations, ACE-FTS data are included to support the F_y budget evaluation (see Section 4.1) as well as to offer a global picture of F_y trends, thus supporting the reanalysis intercomparison.

Originally planned for a 2-year mission (Bernath et al., 2005), the successful SCISAT satellite, launched on August 12, 2003, has been orbiting the Earth and recording infrared solar occultation spectra for more than 17 years now. The three inorganic fluorine reservoirs, HF, COF_2, and COClF, are currently retrieved from ACE-FTS observations. Satellites benefit from a better geometry of observation (i.e., limb sounding in the case of ACE-FTS) compared to ground-based instruments and, consequently, molecules having very weak infrared absorption as COClF can be retrieved. HF retrievals are available from 12 to 54 km, COF_2 from 12 to 34 km, and COClF from 13 to 24 km. Below these altitudes, the abundances of these stratospheric

reservoirs are expected to be negligible (e.g., Nassar et al., 2006; Zander et al., 1992). Therefore, the ACE-FTS partial columns discussed in Section 4 are computed over these altitude ranges and do not involve any extrapolations to the surface. We use version 4.0 of ACE-FTS and we filter outliers following the method detailed in Sheese et al. (2015). Zonal mean trends are obtained from interpolations of the ACE-FTS retrievals from their constant altitude vertical grid to a constant vertical pressure grid employing a mass-conservative regridding method (see, e.g., Section 3.1 in Langerock et al., 2015 or Section 3.1.1 in Bader et al., 2017) followed by binning into 5° latitude intervals (e.g., Steffen et al., 2019). When compared to the ground-based FTIR time series, we use all ACE-FTS measurements included between 40°–50°S and 40°–50°N for Lauder and Jungfraujoch, respectively.

3.3. Models

3.3.1. BASCOE CTM

The Belgian Assimilation System for Chemical ObsErvation chemistry transport model (BASCOE CTM; Chabrillat et al., 2018; Errera et al., 2019; Skachko et al., 2016) is included in this study to compare the representation of the BDC changes (see Section 1) in modern reanalyses (i.e., ERA-Interim, ERA5, JRA55, MERRA, and MERRA-2; see Fujiwara et al., 2017 for a technical comparison of these reanalyses except ERA5; and Hersbach et al., 2020 for a comparison between ERA-Interim and ERA5). Its advection module is the flux-form semi-Lagrangian scheme (FFSL; Lin & Rood, 1996), configured as recommended in Rotman et al. (2001).

Chabrillat et al. (2018) conducted a comparison of advective transport in these reanalyses (except ERA5) through mean age of air evaluations performed by BASCOE CTM. In such a comparison the transport model is used as a transfer tool to accomplish a fair comparison between the reanalyses. The transport module of BASCOE and reanalysis forcing set-up is configured as in the study of Chabrillat et al. (2018). As the comparison of the transport changes represented in reanalyses is one of the main objectives of this research, the reanalysis pre-processing and driving methods are briefly described here again. BASCOE CTM is a kinematic transport model and is therefore only driven by the surface pressure and horizontal wind fields of the reanalyses. It is actually the FFSL algorithm that derives the vertical winds from mass conservation. The algorithm requires the input fields to be staggered on a relatively low-resolution Arakawa-C grid (2° × 2.5° latitude-longitude) while the native vertical grid of each reanalysis is kept. Thus a pre-processing method to carefully transfer the reanalysis spectral or high-resolution fields to the low horizontal grid is needed. Moreover, data assimilation processes used in the elaboration of reanalyses may lead to dynamical imbalances or spurious surface pressure increments that may, in turn, cause serious deteriorations of the BDC (Chabrillat et al., 2018, and references therein). The pre-processor used for BASCOE filters out these dynamical imbalances by evaluating the zonal and meridional wind fields on the low-resolution grid directly from the primitive variables of the spectral dynamical cores (i.e., vorticity and divergence) while correcting for inconsistencies in the pressure increments compared with the divergence fields. This pre-process is directly applied on ERA-Interim and ERA5 spherical harmonics coefficients of vorticity, divergence, and surface pressure (for which the method was originally developed). For the other reanalyses (JRA-55, MERRA, and MERRA-2), we first have to derive these coefficients. For all reanalyses, the spectral coefficients are truncated at wave number 47 to avoid aliasing on the lower resolution grid.

For this study, the chemical scheme of BASCOE CTM is the same expanded scheme as used in Prignon et al. (2019). It includes 65 chemical species interacting through 174 gas-phase reactions, 9 heterogeneous reactions, and 60 photolysis reactions. The expansion of the scheme was made to include HFC species and their corresponding reactions because they are not included in other work based on the BASCOE chemical scheme (Errera et al., 2019; Huijnen et al., 2016; Ménard et al., 2020). The chemistry schemes related to the transformation of organic fluorine sources into inorganic fluorine reservoirs are simplified in BASCOE CTM. Consequently, rather than reacting through the main fluorine reservoirs (HF, COF_2, and COClF), the fluorine atoms, released by the degradation of halocarbons, are directly converted into the total inorganic fluorine tracer F_y (Equation 1). The lower boundary conditions for gas concentrations are taken from the "Historical Greenhouse Gas Concentrations" (HGGC), published by Meinshausen et al. (2017) in the framework of the Climate Model Intercomparison Project Phase 6 (CMIP6) experiments, and their extension for the years 2016–2018 (using scenario SSP2-4.5; Meinshausen et al., 2020). The initial state (December

1, 1984) of all simulations is based on a BASCOE reanalysis of Aura MLS (Microwave Limb Sounder) for the year 2010 that was scaled by global constants to obtain surface concentrations representative of 1984 (Prignon et al., 2019).

The five simulations used here include the daily varying spectral solar irradiance as recommended for the Coupled Model Intercomparison Project Phase 6 (CMIP6; Matthes et al., 2017). The AoA derived from ERA-Interim, MERRA, MERRA-2, and JRA-55 by the BASCOE CTM (Chabrillat et al., 2018) apply exactly here because the grid and transport settings are strictly identical: time step set to 30 min, a 2° × 2.5° latitude-longitude grid and the native hybrid sigma-pressure vertical grids of the driving reanalyses.

3.3.2. TOMCAT

TOMCAT/SLIMCAT (hereafter TOMCAT; Chipperfield, 2006) is a global CTM that can be used in a variety of configurations. In this study, it is used with a detailed stratospheric chemistry scheme to calculate the partitioning of F_y species. The model chemistry scheme includes the main species of the O_x, NO_y, Cl_y, Br_y, HO_x, and CHO_x chemical families, along with long-lived source gases. The TOMCAT F_y chemistry is as described in Harrison et al. (2014, 2016) who compared the model with ACE-FTS HF, COF_2, and COClF. COF_2 is assumed to be produced from the degradation of CFC-12, CFC-113, CFC-114, CFC-115, HCFC-22, HCFC-142b, HFC-23, HFC-134a, HFC-152a, Halon 1211, and Halon 1301, with COClF production from the degradation of CFC-11, CFC-113, and HCFC-141b. A very small amount of HF is assumed to form directly from the source gases, mainly arising from HFC-134a (Harrison et al., 2016). The primary loss of COF_2 and COClF in the stratosphere occurs via photolysis, with an additional secondary loss mechanism through reaction with $O(^1D)$.

In this study, TOMCAT was run at a horizontal resolution of 2.8° × 2.8° with 32 levels from the surface to approximately 60 km in a setup similar to that used by Dhomse et al. (2019). The model used a hybrid sigma-pressure vertical coordinate and was forced by ECMWF ERA-Interim meteorological fields. The simulation was initialized in 1977 and uses specified global mean surface mixing ratios of the long-lived source gases from the 2018 WMO Ozone Assessment (WMO, 2018). The model also includes solar flux and aerosol Surface Area Density variations as described in Dhomse et al. (2015, 2016).

3.4. Trend Methods

Trend estimates presented in this research are obtained from a classic linear trend model accounting for an annual cycle:

$$y_t = d_t + s_t + u_t, \tag{3}$$

with

$$d_t = \alpha + \beta t, \tag{4}$$

and

$$s_t = \sum_{j=1}^{S} a_j \cos\left(2j\pi t\right) + b_j \sin\left(2j\pi t\right), \tag{5}$$

where y_t is the observation or model values at time t, d_t is a simple linear trend model with α its intercept and β is the slope we are looking for, s_t is a Fourier series of degree S modeling the annual cycle of the time series, and u_t is a stochastic error term. Accounting for the annual cycle with a Fourier series for atmospheric time series has already been proposed in a number of previous studies (e.g., Franco et al., 2015; Friedrich, Beutner, et al., 2020; Gardiner et al., 2008; Mahieu et al., 2017; Prignon et al., 2019). From these studies, it appears that using a third-order Fourier series ($S = 3$) allows to correctly capture the intra-annual seasonality of such time series. Tests with our data set led us to the same conclusion (not shown). The error term u_t in Equation 3 can exhibit heteroskedasticity (i.e., changing variance over time; see Section S1) and autocorrelation, as often observed in geophysical time series (Friedrich, Beutner, et al., 2020). Therefore, once a model such as the one described in Equation 3 is fit to the data, a method to obtain a measure of uncertainty around the resulting estimates has to be found that is valid for this error specification.

Gardiner et al. (2008) proposed a bootstrap residual resampling method to assess trend uncertainties that was further applied in subsequent studies (e.g., Franco et al., 2015; Mahieu et al., 2014). Briefly, after fitting the model of Equation 3 to the time series, the residuals thus obtained are resampled randomly at each time t and

a trend is computed again on the new time series. This process is repeated x times and a distribution of trend values is obtained. Finally, the percentiles of this trend distribution are used to quantify the uncertainty around the trend estimate. While this method is very convenient as it does not require an assumption of normality, it, however, fails at preserving the potential autocorrelation and heteroskedasticity of the residuals as they are resampled fully at random. Other studies (e.g., Prignon et al., 2019; Vigouroux et al., 2018; Zhou et al., 2018) applied the method of Santer et al. (2000) to correct for autocorrelation when calculating the standard errors of the trend estimates. However, explicitly correcting for autocorrelation in this way creates additional estimation uncertainty which is not taken into account by this method. In conclusion, it thus appears that both methods of Gardiner et al. (2008) and Santer et al. (2000) might not be adequate for geophysical time series.

In the face of this issue, we apply here the autoregressive wild (ARW) bootstrap method (e.g., Friedrich, Beutner, et al., 2020; Friedrich, Smeekes, & Urbain, 2020). This modified bootstrap method is well-established in the econometric literature and was recently applied to ground-based FTIR retrievals of ethane (Friedrich, Beutner, et al., 2020). The ARW bootstrap offers three major advantages compared to the previously described methods: it is applicable to (a) heteroskedastic and (b) autocorrelated time series presenting non-negligible (c) missing observations. This last issue is indeed a common feature in ground-based FTIR observations as the technique requires clear sky conditions (see Section 3.1), causing the missing data pattern to be unpredictable.

Contrary to the residual resampling described in Gardiner et al. (2008), the wild bootstrap does not perform any residual permutations and simply generates bootstrap errors and observations as:

$$z_t^* = \xi_t^* \hat{z}_t, \tag{6}$$

$$y_t^* = \hat{y}_t + z_t^*, \tag{7}$$

where z_t^* is the bootstrap error at time t, $\hat{z}_t$ is the residual of the fit of our linear trend model at time t, ξ_t^* is an independent and identically distributed random variable, with an expectation of 0 and a variance of 1, generated for each observation, $\hat{y}_t$ is the value predicted by our linear trend model at time t and y_t^* is the bootstrap observation. Bootstrap time series built this way are again generated a large number of times (here we perform 25,000 bootstrap iterations) to obtain a distribution of trends by applying the trend estimator to each of these series. The wild bootstrap method needs to be further modified in situations with autocorrelation since the independence of the random variables $\left\{\xi_t^*\right\}$ destroys the dependence pattern which is present in the residuals. The ARW bootstrap generates the random variables $\{\xi_t^*\}$ as an autoregressive process of order 1 (AR(1)):

$$\xi_t^* = \gamma \xi_{t-1}^* + v_t^*, \tag{8}$$

where γ is the AR(1) parameter and v_t^* is an independent and identically distributed random variable with an expectation of 0 and a variance of $1 - \gamma^2$. The bootstrap errors and observations are then generated following Equations 6–8. Since the $\{\xi_t^*\}$ are not independent anymore, this ARW bootstrap method will capture some of the autocorrelation of the time series while preserving its heteroskedasticity. The choice of γ constitutes a trade-off between allowing for variation in the bootstrap samples (small γ values, falling back to the wild bootstrap) and capturing more autocorrelation ($\gamma \to 1$; Friedrich, Beutner, et al., 2020). The parameter γ can either be chosen (thus acting as a tuning parameter) or determined as a function of the sample size n. We follow the latter case and, as suggested by Smeekes and Urbain (2014), Friedrich, Beutner, et al. (2020), and Friedrich, Smeekes, & Urbain (2020), let $\gamma = 0.01^{1/l}$, with $l = 1.75n^{1/3}$.

Finally, several time series in this study display smoothed trend lines that are obtained using the nonparametric trend estimation technique described in Friedrich, Beutner, et al. (2020) and Friedrich, Smeekes, & Urbain (2020). While the linear trend model restricts the trend to be of linear shape, the advantage of the nonparametric approach is that it gives an idea of the underlying time trend without requiring such a functional form specification. At each point in the sample, this method locally approximates the underlying trend by calculating a weighted average of neighboring observations. How many observations are included in this weighted average is determined by a bandwidth parameter, h, expressed as a fraction of the sample size. To obtain the desired sensitivity to the interannual variation, the latter parameter can be chosen by the user, depending on the context of the study. Friedrich, Smeekes, & Urbain (2020) also proposed a

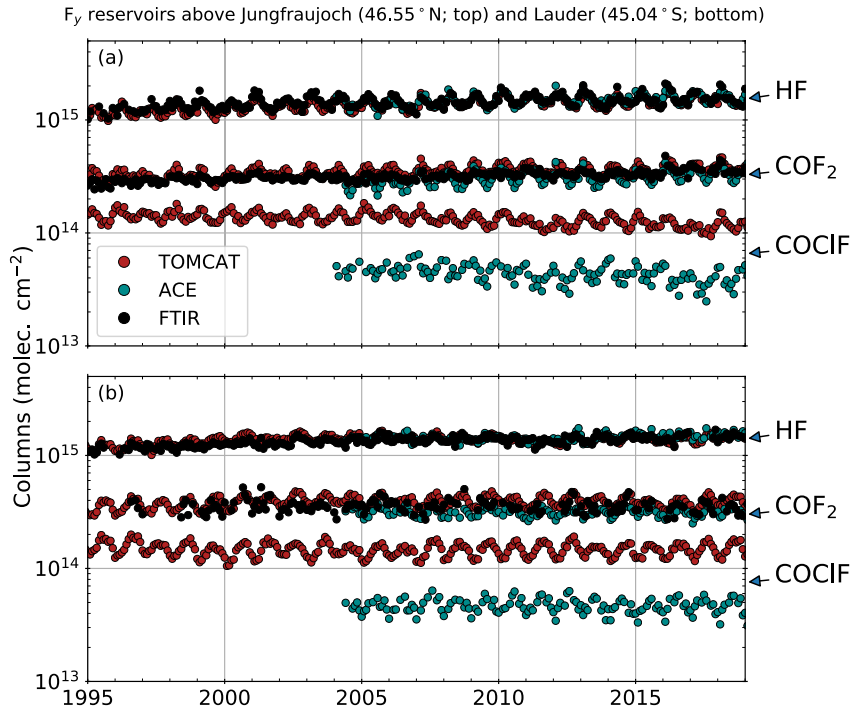

Figure 2. Total columns (molec. cm^{-2}) of total inorganic fluorine (F$_y$) reservoirs observed above Jungfraujoch (a) and Lauder (b) by ground-based (black) and ACE-FTS (dark cyan) Fourier transform spectrometers as well as simulated by TOMCAT (red). Note that COClF is currently not retrieved at either ground-based station (see Section 3.1).

data-driven procedure to determine the bandwidth parameter. Here, we manually chose $h = 0.1$ to reasonably smooth the time series while preserving the sought multiyear variability.

Note that the given time periods for trend estimations include the starting and ending years, for example, 2004–2018 corresponds to a 15-year period from January 2004 to December 2018.

3.5. Modified Normalized Mean Bias

The mean relative differences of this study are expressed in term of modified normalized mean bias (MNMB), following Equation 1 in Eskes et al. (2015):

$$\mathrm{MNMB} = 100\,\% \times \frac{1}{N}\sum_i^N \frac{x_i - y_i}{\left(x_i + y_i\right)/2}, \tag{9}$$

with N is the number of coincidences between both x and y data sets. MNMBs are given along with their 1σ standard deviation.

4. Inorganic Fluorine Above Jungfraujoch and Lauder

4.1. Partitioning of Total Inorganic Fluorine F$_y$ and Marginal Contribution of COClF

Figure 2 shows the time series of the total columns of the three major inorganic fluorine reservoirs above Jungfraujoch and Lauder. The ground-based FTIR retrievals of HF and COF$_2$ exhibit a very good agreement with both the retrievals of ACE-FTS and the outputs from TOMCAT. With respect to COClF no FTIR retrievals are available but we note large differences between the ACE-FTS retrievals and the TOMCAT results. Table 1 displays the MNMB over the 2004–2018 period and the associated uncertainties. These MNMBs are computed over monthly average coincidences. For HF, there are 144 (8.5 months/year on average) and 138 (8.5 months/year) coincidences between ACE-FTS and the FTIR observations at Jungfraujoch and Lauder, respectively. For COF2, these numbers are 137 (8.5 months/year) and 96 (6 months/year). While the biases between the HF data sets are negligible and the larger biases between COF$_2$ data sets

Table 1
Relative Difference (MNMB, Equation 9) Between ACE-FTS and FTIR, and Between ACE-FTS and TOMCAT, for Monthly Average Coincidences of Total Columns of the Three Major Inorganic Fluorine Reservoirs, Above Jungfraujoch and Lauder and for the Period 2004–2018

		Lauder		Jungfraujoch	
2004–2018		FTIR	TOMCAT	FTIR	TOMCAT
ACE FTS	HF	2.79 ± 7.4%	2.74 ± 7.5%	−0.32 ± 7.8%	4.21 ± 6.2%
	COF_2	−9.82 ± 12%	−22.4 ± 6.6%	−8.08 ± 11%	−16.5 ± 8.5%
	COClF	n.a.	−102 ± 8%	n.a.	−98.1 ± 12%

Note. Negative values indicate lower ACE-FTS total columns. See Section 3.5 for the definitions of MNMB and the associated uncertainties. ACE-FTS, Atmospheric Chemistry Experiment Fourier Transform Spectrometer; HF, hydrogen fluoride; MNMB, modified normalized mean bias.

remain within the large systematic errors assessed for ground-based retrievals (reaching 20% due to large spectroscopic uncertainty; see Section 3.1.2), the large biases between the ACE-FTS and TOMCAT data sets indicate a systematic disagreement for COClF that is also noted and discussed in Harrison et al. (2016). This bias is thought to be caused by an underestimation of COClF loss processes resulting in a too long COClF lifetime in the model (Harrison et al., 2016).

Figure 3 depicts the time series of F_y as computed from the reservoir time series of Figure 2 (see Equations 1 and 2). The F_y simulation of BASCOE CTM driven by ERA-Interim is also displayed for comparison. Despite the systematic difference between TOMCAT and BASCOE CTM, we show here that both model time series present an almost identical interannual variability, thus giving confidence in the forcing methods of BASCOE CTM. Regarding the F_y partitioning above both stations, from ACE-FTS retrievals, we compute that HF represents 69.6% and 68.4% of F_y at Jungfraujoch and Lauder, respectively. TOMCAT simulates a lower relative contribution of HF to F_y, with HF ratio representing 60.2% and 58.7% at the two stations.

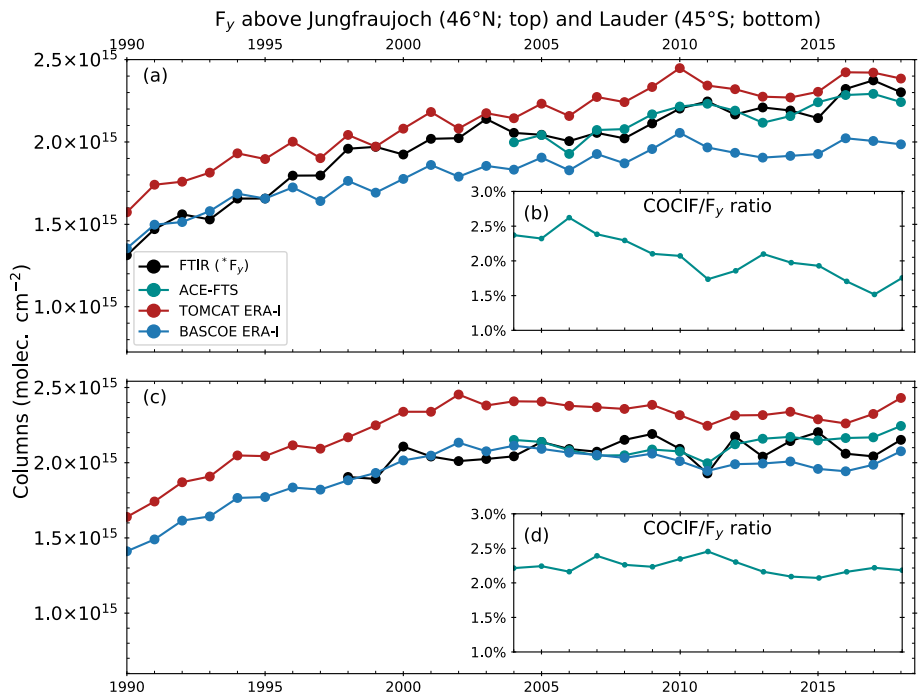

Figure 3. Annual means of the total inorganic fluorine (F_y) total columns (molec. cm^{-2}) observed above Jungfraujoch (a) and Lauder (c) by ACE-FTS (dark cyan) or simulated by TOMCAT (red) and BASCOE CTM (blue). FTIR total columns (black) do not include COClF (see Section 3.1) and correspond to $^*F_y$ (Equation 2). Panels (b) and (d) depict the contribution of COClF to F_y (%) computed from ACE-FTS time series.

The corresponding fractions for COF_2 (note that COF_2 total columns are multiplied by 2 to compute the F_y budget, see Equation 1) are 28.4% and 29.4% (ACE-FTS above Jungfraujoch and Lauder, respectively) and 33.0% and 34.1% (TOMCAT above Jungfraujoch and Lauder, respectively). Thanks to the success of the Montreal Protocol, chlorinated source gas emissions have now been declining for several decades (WMO, 2018). As a result, COClF is decreasing in the atmosphere while HF and COF_2 are not, leading to a decreasing contribution of COClF to F_y. From ACE-FTS time series we note, however, that between 2014 and 2018 the contribution of COClF has decreased by less than 1% above Jungfraujoch (Figure 3b) and remained constant above Lauder (Figure 3d). To evaluate the impact of the decreasing contribution of COClF to F_y, we have estimated ACE-FTS trends of F_y and $^*F_y$ (see Equations 1 and 2, respectively) for the period 2004–2018. We noted only a marginal difference between F_y and $^*F_y$ trends (not shown) which is negligible when compared to the estimated uncertainty of these trends (as given by the ARW bootstrap method, see Section 3.4).

In conclusion, we have shown that omitting COClF in the F_y budget should not induce large biases as HF and COF_2 are taken together to represent at least 93% (from TOMCAT), and even up to 98% (from ACE-FTS), of the closed F_y budget. The remaining contribution of COClF is moreover sufficiently stable over time to not induce any significant bias in the estimation of the F_y trend when it is approximated by the $^*F_y$ trend. Consequently, all trends of ACE-FTS in the following sections are computed over $^*F_y$ time series.

4.2. Inorganic Fluorine Time-Series

In Figure 4, we show the time series of $^*F_y$ observed by FTIR and ACE-FTS and F_y simulated by the BASCOE CTM above both NDACC stations. These time series are shown individually in Figures S1 and S2 (along with the uncertainties estimated for the monthly means and nonparametric trend lines). As already demonstrated in Figures 2 and 3, ground-based FTIR and ACE-FTS retrievals are in good agreement at Lauder and Jungfraujoch (Figures 4a and 4b, respectively).

F_y simulations performed by BASCOE CTM driven by five modern reanalyses show large differences in absolute values and trends (Figures 4e and 4f). At both stations, MERRA-2 delivers the highest F_y columns, ERA-Interim and JRA-55 the lowest ones, with MERRA and ERA5 situated in between.

Relative differences (MNMB, see Equation 9) between observations and BASCOE CTM simulations computed on 2004–2018 monthly mean coincidences are shown in Table 2. For the Jungfraujoch there are 168 coincident months (11 months/year on average) with the BASCOE CTM time series, for Lauder there are 107 coincident months (7 months/year on average). While observations show an overall good agreement at both sites, the performance of the BASCOE CTM depends on the forcing reanalysis and the evaluated station. It should also be noted that the close agreement between ground-based FTIR and ACE-FTS $^*F_y$ time series at Lauder is caused by the cancellation of the HF and COF_2 biases (Table 1).

5. Trends

5.1. Long-Term Trends

We now present an analysis, summarized in Figures 5 and 6, of the long-term trends computed from observations (ground-based FTIR and ACE-FTS) and BASCOE CTM simulations. We compute the trends, along with their uncertainties, on daily values when available, that is, except for the Lauder ground-based FTIR time series (see Section 3.1). The effect of the sampling (daily vs. monthly values) was investigated and does not change significantly the value of the trends presented here (not shown). The longest time period for which all data sets are available is 2004–2018 (except for MERRA which ends at the end of 2015). We determine trends over three time periods:1990–2018, 1990–1999, and 2004–2018. 2004–2018 was chosen instead of 2000–2018 such as to accommodate the full ACE-FTS time range. We use the method described in Section 3.4 to assess the uncertainty around the estimated trends. This method is valid for residuals showing heteroskedasticity and autocorrelation. The heteroskedasticity of the residuals is further discussed in Section S2.

We first consider the trends computed above Lauder and Jungfraujoch (Figures 5a and 5b, respectively). For the longest time period 1990–2018, covered by the Jungfraujoch ground-based observations and BASCOE

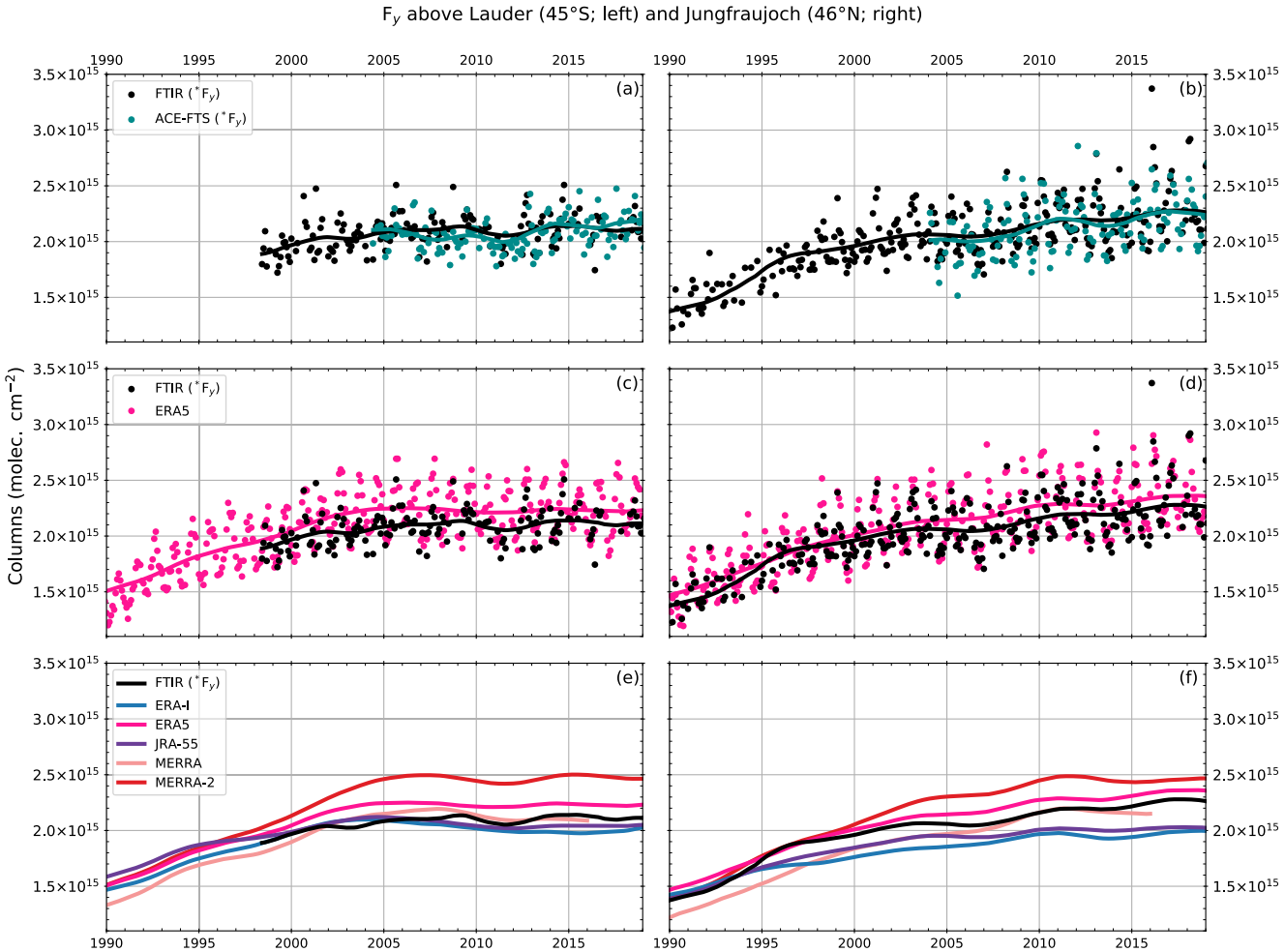

Figure 4. Inorganic fluorine above Lauder (left panels a, c, e) and Jungfraujoch (right panels b, d, f). Panels (a and b) are observations from ground-based FTIR (black) and ACE-FTS (at site latitude ±5°; dark cyan). For a direct comparison between observations, COClF is excluded from the inorganic fluorine of ACE-FTS (see Section 4.1). Panels (c–f) are the BASCOE CTM total inorganic fluorine simulations driven by the five reanalyses (ERA-Interim, MERRA, MERRA-2, JRA-55, and ERA5) and interpolated at the gridpoints closest to Lauder (c, e) and Jungfraujoch (d, f). Points are monthly means and lines are nonparametric smoothing trends (see Section 3.4). See Figures S1 and S2 for uncertainties around monthly means and nonparametric smoothing trends, omitted here for clarity.

CTM, the differences qualitatively shown in Figure 4 are confirmed quantitatively: MERRA and MERRA-2 deliver the largest trends while the trends obtained with ERA-Interim (1.85 × 10^{13} molec. cm^{-2} year^{-1}) and JRA-55 (2.01 × 10^{13} molec. cm^{-2} year^{-1}) are the smallest among the five BASCOE CTM simulations and also the closest to the trends derived from the Jungfraujoch FTIR (2.33 × 10^{13} molec. cm^{-2} year^{-1}). Yet a separate inspection of the early (pre-2000) and recent (post-2000) periods delivers very different results. During the period of strongly increasing F$_y$ 1990–1999, the ERA-Interim reanalysis delivers a trend value

Table 2
*2004–2018 Relative Difference (MNMB, Equation 9) Between Jungfraujoch (JFJ) and Lauder FTIR *F$_y$, and ACE-FTS *F$_y$ and BASCOE CTM F$_y$ Driven by ERA-Interim, ERA5, JRA-55, MERRA (Ending in 2015), and MERRA-2*

2004–2018	ACE-FTS	ERA-I	ERA5	JRA-55	MERRA	MERRA-2
FTIR JFJ	2.66 ± 12.9%	12.43 ± 5.2%	−2.59 ± 6.3%	9.66 ± 5.4%	3.58 ± 6.9%	−9.25 ± 5.2%
FTIR Lauder	1.08 ± 7.3%	2.88 ± 6.6%	−6.96 ± 6.7%	1.19 ± 6.0%	−2.62 ± 7.4%	−16.87 ± 6.4%

Note. See Section 3.5 for the definitions of modified normalized mean bias (MNMB) and the associated uncertainties. ACE-FTS, Atmospheric Chemistry Experiment Fourier Transform Spectrometer.

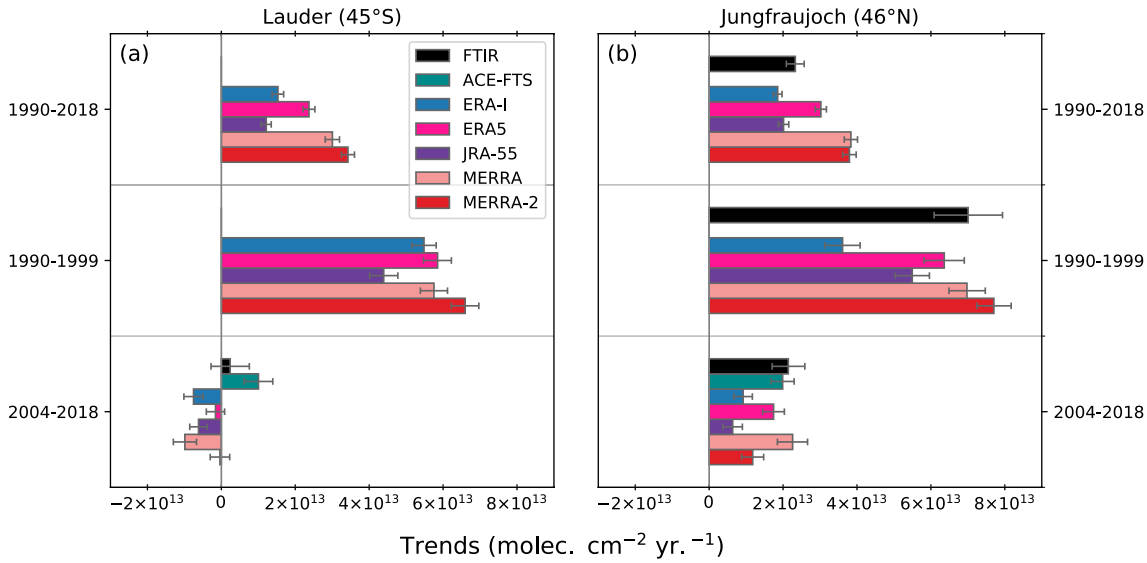

Figure 5. Inorganic fluorine trends above Lauder (a) and Jungfraujoch (b) computed for ground-based FTIR and ACE-FTS observations (*F_y) as well as for BASCOE CTM simulations (F_y). Horizontal thin error bars are the 95% uncertainty range around estimated trend values. Note that MERRA ends in December 2015.

at Jungfraujoch that is half as large as the FTIR observations. This significant underestimation is not reproduced by the BASCOE CTM simulation driven by the most recent ECMWF reanalysis, ERA5, and is not found with the three other CTM simulations. Regarding the 2004–2018 common time period, large differences are depicted between both sites as well as between data sets (especially between reanalyses) at each site. At Jungfraujoch, ground-based and ACE-FTS time series reveal an excellent agreement. At Lauder, FTIR and ACE-FTS trends are not significantly different as their uncertainties overlap. An important result for this period is that observations and model simulations exhibit significantly higher trend values at Jungfraujoch than at Lauder. Additionally, all trends from BASCOE-CTM simulations are too low in comparison to observations at Lauder, even significantly negative for ERA-Interim and JRA-55 (the trend obtained with MERRA is also negative but over a different period that ends in 2015).

Trends computed from zonal mean time series (Figure 6) expand these results to the whole stratosphere. During the 1990s, MERRA, MERRA-2, and ERA5 deliver comparable trend values while those obtained from ERA-Interim and JRA-55 are much lower. For the common data set period, 2004–2018 (except for MERRA, ending in 2015), interhemispheric differences in the lower stratosphere on zonal mean trends are noticeable, with larger trend values in the Northern Hemisphere than in the Southern Hemisphere. While ACE-FTS trends also show larger values for the Northern Hemisphere, the values for the Southern Hemisphere are not statistically significant at the 95% confidence level.

5.2. On the Dipole Interhemispheric Pattern of Shorter Timescale Trends

We highlighted in Section 1 a body of studies reporting on the interhemispheric asymmetries in trends of long-lived tracers or AoA. In this section, we investigate our inorganic fluorine time series for these short-term modulations that are related to BDC changes. Strahan et al. (2020, Figure 3) highlighted a periodic signal in the time series of interhemispheric differences for deseasonalized AoA as well as for deseasonalized long-lived tracers (i.e., HNO_3 and HCl). From 1995 to 2018, 2011 stands out as the year with the strongest interhemispheric difference in their three analyzed data sets, with AoA and tracer anomalies much smaller in the Southern Hemisphere than in the Northern Hemisphere. The years 2005 and 2014, on the other hand, stand out as years with opposite interhemispheric differences, that is, AoA and tracer anomalies that are larger in the Southern Hemisphere than in the Northern Hemisphere. Based on this observation, we expect to find that the interhemispheric asymmetries in our inorganic fluorine trends are clearest for the period 2004–2011. Due to the relatively short time series considered for this section, we emphasize that

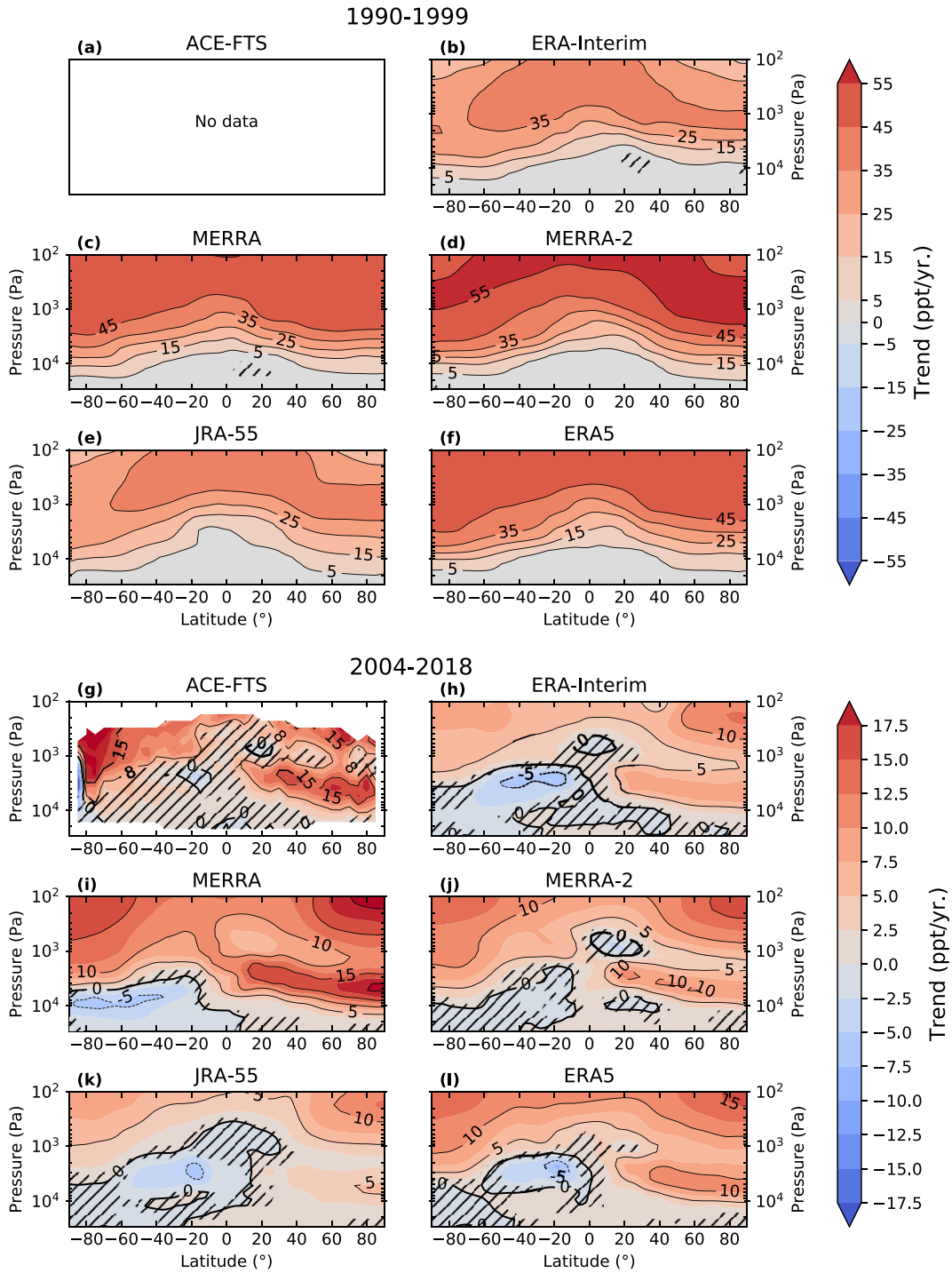

Figure 6. Long-term trends of *F_y (ACE-FTS) and F_y (BASCOE CTM forced by ERA-Interim, MERRA, MERRA-2, JRA-55, and ERA5) for 1990–1999 (a–f) and 2004–2018 (g–l). Hatched areas indicate grid points where the trend is not significant at the 95% confidence level. Note that MERRA ends in December 2015. Note the different color scales for the early and later periods.

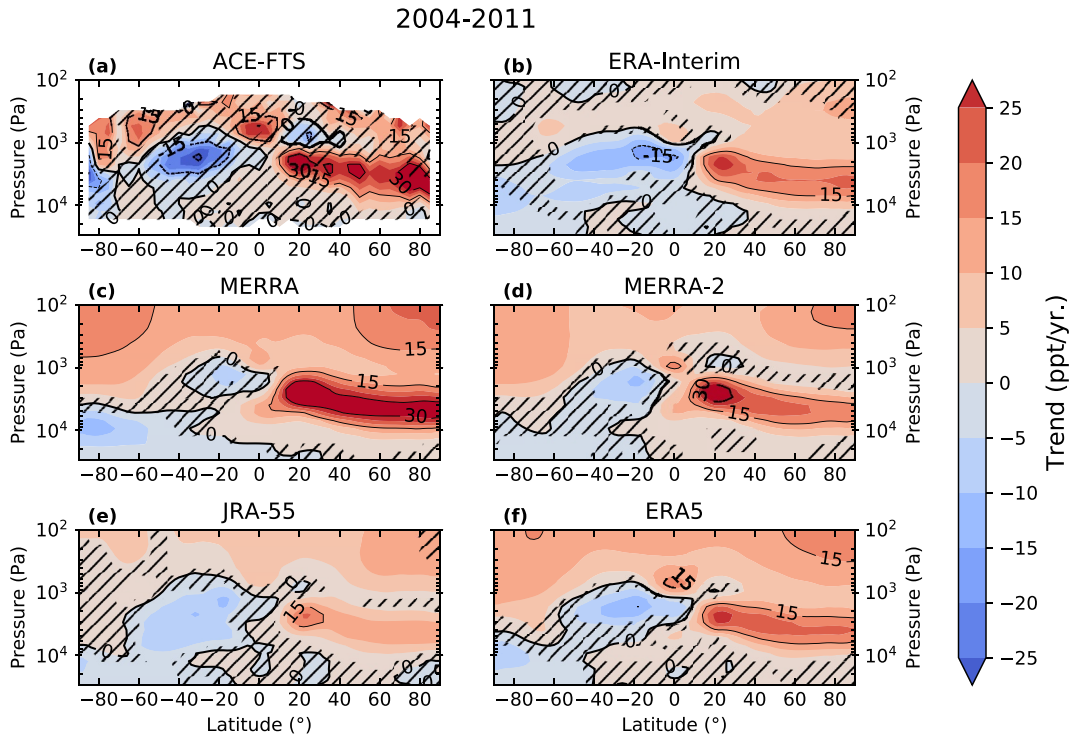

Figure 7. Trends of *F_y (ACE-FTS) and F_y (BASCOE CTM forced by ERA-Interim, MERRA, MERRA-2, JRA-55, and ERA5 for 2004–2011. Hatched areas indicate grid points where the trend is not significant at the 95% confidence level.

the following shorter-term trend analysis is focused on the interhemispheric asymmetries rather than the computed absolute trend values.

As expected, a clear and significant hemispheric asymmetry in *F_y trends is found from ACE-FTS observations for the period 2004–2011, with positive trend values in the Northern Hemisphere and negative trend values in the Southern Hemisphere (Figure 7a). The negative *F_y trend of the Southern Hemisphere is unexpected as organic fluorine sources are accumulating linearly in the troposphere during this period (Figure 1). In the Northern Hemisphere, the positive trend area stretches from around 10°N up to the pole with a vertical extent from 100 to 10 hPa. In the Southern Hemisphere, the area with negative trends is more limited than in the Northern Hemisphere, ranging from 20°to −50°S and from 20 to 10 hPa. Moreover, a second negative trend area is seen above the South Pole. All reanalyses reproduce well the spatial pattern depicted by ACE-FTS in the Northern Hemisphere but the interhemispheric differences are not as clear as in the observations because the negative trends in the Southern Hemisphere are weaker and not significant in the case of MERRA (Figure 7c).

From ground-based FTIR retrievals, we also note contrasting *F_y trend values between Lauder and Jungfraujoch for the period 2004–2011. The trends are 3.23 (2.4–4.1) × 10^{13} molec. cm^{-2} $year^{-1}$ at Jungfraujoch and −0.43 (−1.9 to 1.1) × 10^{13} molec. cm^{-2} $year^{-1}$ at Lauder, that is, a non-significant trend at Lauder (45°S) and a large positive trend at Jungfraujoch (46°N). ACE-FTS shows even more contrasting results. In the Northern Hemisphere midlatitudes (40°–50°N), the total column trend is 3.42 (2.6–4.2) × 10^{13} molec. cm^{-2} $year^{-1}$. In the Southern Hemisphere midlatitudes (40°–50°S), it is −1.63 (−2.4 to −0.9) × 10^{13} molec. cm^{-2} $year^{-1}$.

6. Discussion

The analysis of inorganic fluorine time series and their long-term trends highlights substantial differences between the reanalyses. From Figures 4–6, it is, as one would expect, clear that large F_y trend values (i.e., MERRA and MERRA-2) result in higher F_y values in simulated time series and inversely for low trend

values (i.e., ERA-Interim and JRA-55). A comparison of this result with AoA studies can be drawn. In both studies of Chabrillat et al. (2018) and Ploeger et al. (2019), MERRA-2 is the reanalysis with the oldest AoA while JRA-55 and ERA-Interim, being close to each other, have the youngest AoA. MERRA, which is only compared in Chabrillat et al. (2018), has a mean AoA that is slightly younger than MERRA-2. An older mean AoA in the midlatitudes means a longer transit time from the tropical tropopause to the midlatitudes (i.e., slower residual circulation) and/or more time spent in large-scale eddies (i.e., irreversible mixing) in the midlatitudes. In the case of F_y, longer transit to—or residency times in—the midlatitudes allow for larger fraction of the source gases to be converted into inorganic fluorine reservoirs (i.e., HF, COF_2, and COClF; see Section 2). Hence, the older AoA obtained from MERRA-2 is directly responsible for the larger F_y total columns when this reanalysis is used to drive BASCOE CTM and the steeper AoA trends with MERRA-2 are reflected in the stronger F_y trends obtained with that reanalysis. The same reasoning applies to the other reanalyses since their respective mean AoA, as determined by Chabrillat et al. (2018), are identical in this study (see Section 3.3.1).

Long-term trend analysis of the FTIR observations at Jungfraujoch also revealed significantly smaller trends of $*F_y$ for the period 2004–2018 than for the period 1990–1999. This is reproduced by all CTM simulations, independently of the driving reanalysis (Figures 5 and 6). From HF satellite observations and a TOMCAT/SLIMCAT ERA-Interim driven simulation, Harrison et al. (2016) also noted larger trend values during the end of the 20th century (1991–1997) than the beginning of the 21st century (2004–2012). This reduced inorganic fluorine trend for the 21st century is expected as the total organic fluorine growing rate at surface peaked in the early 1990s (Figure 1). Interestingly, all reanalyses except ERA-Interim show comparable trend values at Jungfraujoch and at Lauder for the period 1990–1999 (Figure 5). Indeed, at Jungfraujoch, the BASCOE CTM simulation driven by ERA-Interim produces F_y trend values that are too small compared to ground-based FTIR observations and the other BASCOE CTM simulations. Harrison et al. (2016) also noted a disagreement for this period between HF global trends from their SLIMCAT run driven by ERA-interim and from HALOE (HALogen Occultation Experiment) satellite observations, with ERA-Interim trend being too small compared to that from HALOE. An unrealistic representation of the stratospheric dynamics in ERA-Interim near the end of the 20th century is likely producing biased F_y trends (Harrison et al., 2016). The new ECMWF reanalysis, ERA5, does not reproduce this bias and thus, seems more appropriate to drive BASCOE CTM for our F_y simulations compared to the former ERA-Interim reanalysis.

A key result of this study is the statistically smaller inorganic fluorine trend values at Lauder than at Jungfraujoch for all data sets for the period 2004–2018 (Figures 5 and 6). Ground-based FTIR and ACE-FTS trend values are in agreement at both stations. At Lauder, all BASCOE CTM simulations show small F_y trend values for this period with even negative values for ERA-Interim and JRA-55. As noted in the introduction (Section 1), using NDACC ground-based FTIR measurements, Strahan et al. (2020) also noted smaller HNO_3 and HCl trend values in the Southern Hemisphere compared to the Northern Hemisphere for the period 1994–2018. Moreover, estimating interhemispheric AoA trends from the NDACC measurement interhemispheric trends (see Section S1 in Strahan et al., 2020) as well as using a GMI CTM AoA simulation driven by MERRA-2, they concluded that the HNO_3 and HCl interhemispheric differences in trend were caused by a relative strengthening of the BDC (corresponding to lower AoA values) in the Southern Hemisphere. Indeed, they found that the AoA in the southern extratropical lower stratosphere has been getting younger relative to the Northern Hemisphere at a mean rate of 1 month/decade for the past 25 years, with most of the change occurring in the Southern Hemisphere. While we do not assess any AoA trends in the present study, a comparison with our results showing lower F_y trend values in the Southern Hemisphere than in the Northern Hemisphere for the 21st century, supports the conclusions of Strahan et al. (2020), using another long-lived trace gas reservoir.

By subtracting each respective non-parametric fit (see Section 3.4 for methods and lines in Figure 4) of the Northern Hemisphere time series to that of the Southern Hemisphere (e.g., Lauder minus Jungfraujoch FTIR or ACE-FTS 40°–50°S minus ACE-FTS 40°–50°N), Figure 8 mimics Figure 3 in Strahan et al. (2020) and reveals the dynamical signature of the discussed trends as the tropospheric trend of F_y sources should affect both hemispheres equally (Strahan et al., 2020). Figure 8 confirms the overall building-up asymmetry between midlatitudes of both hemispheres in terms of inorganic fluorine and thus AoA for the period 2000–2018. Moreover, it shows again that, despite the noted large differences between reanalyses, all BASCOE

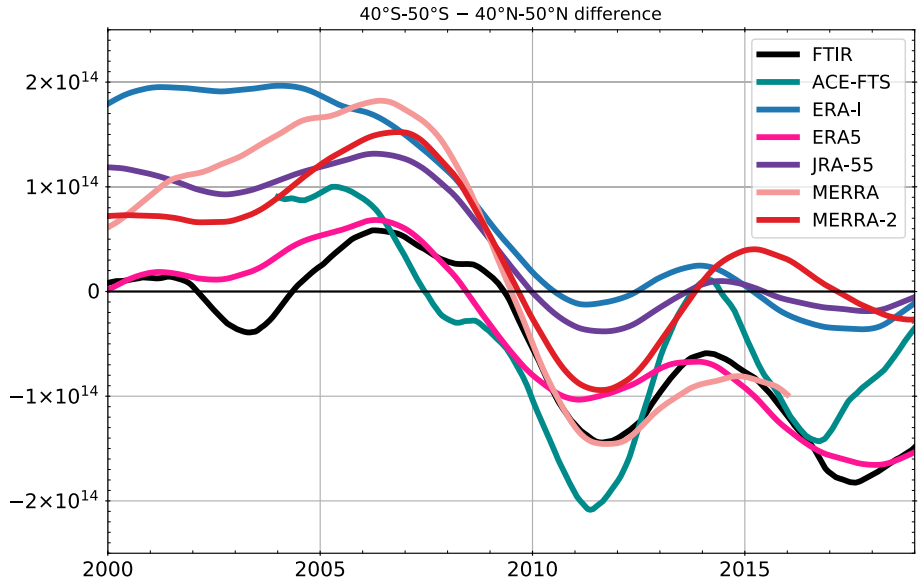

Figure 8. Midlatitude differences (40°–50°S minus 40°–50°N) between respective observations of *F_y (ground-based FTIR and ACE-FTS) and BASCOE CTM simulation of F_y. The ground-based FTIR (black) difference is computed from Lauder (45°S) and Jungfraujoch (46°N). See text in Section 6 for methods.

CTM simulations capture that F_y is accumulating less rapidly in the Southern Hemisphere midlatitudes than in the Northern Hemisphere midlatitudes. Figure 8 furthermore highlights years of strong interhemispheric differences (i.e., 2006–2007, 2011, 2014–2015, and 2017). Here, we note again that all reanalyses reproduce, more or less strongly, the observed (ground-based FTIR and ACE-FTS) 5–7-year interhemispheric variability discussed in Strahan et al. (2020) and more specifically the considerable drop leading to the local minimum of the year 2011, followed by the local maximum of the year 2014. This variability seems to be more strongly reproduced by MERRA and MERRA-2 than by the other reanalyses (Figures 7 and 8).

The dipole structure in trends of the first two decades of the 21st century of long-lived tracers or AoA that has been discussed in the past years (see Section 1 and references therein) is also noted in the trends of inorganic fluorine (Figure 7). The time-period considered, often limited by data availability, is similar among the noted studies, for example, 2002–2012 in Stiller et al. (2012) and Haenel et al. (2015), 2005–2012 in Stiller et al. (2017), or 2002–2015 in Chabrillat et al. (2018) and Ploeger et al. (2019). Moreover, long-lived tracer studies generally limit their CTM simulation to a unique forcing reanalysis, which is often the ERA-Interim reanalysis (e.g., Han et al., 2019; Harrison et al., 2014, 2016; Mahieu et al., 2014; Stiller et al., 2017). As in Strahan et al. (2020), we show here that considering a sufficiently long time period allows for the detection of succeeding minima and maxima in the time series of interhemispheric difference (Figure 8). In this context, the dipole structure in trends of AoA and long-lived tracers first described by Stiller et al. (2012) and Mahieu et al. (2014) and followed by a number of other studies is actually situated between two years of large (actually among the largest) opposite extremes in interhemispheric differences (i.e., 2006–2007, with older AoA in the Southern Hemisphere relative to the Northern Hemisphere, to 2011 or 2012, with younger AoA in the Southern Hemisphere relative to the Northern Hemisphere). On the other hand, the period 2002–2015, chosen by Chabrillat et al. (2018) and Ploeger et al. (2019), might not be adequate to detect this dipole as the local minimum or maximum interhemispheric anomalies are missed by a few years at both limits of the time period. Moreover, these two studies concluded that only ERA-Interim showed a dipole structure in AoA trends (i.e., opposite hemispheric trends) over the 2002–2015 period. Chabrillat et al. (2018) further mentioned that the Northern Hemisphere positive AoA trend was larger and significant at more grid points for the 2002–2012 period. Zonal mean trends computed on our F_y simulations for the period 2002–2015 only show a dipole structure for ERA-Interim (not shown).

While recent studies agree on the role of the QBO in the midlatitude BDC multiyear-variability, it is still unclear if the observed periodicity is actually caused by the same phenomenon or if it is a succession or

alignment of more or less independent phenomena. The QBO itself is inherently unpredictable as it has, on the one hand, a variable period of ~22 to ~36 months (e.g., Osprey et al., 2016) and, on the other hand, an intrinsic variability as illustrated by the unprecedented QBO disruption in 2015–2016 (Diallo et al., 2018; Osprey et al., 2016; Tweedy et al., 2017). In addition to the interaction between the BDC and the QBO, the El Niño–Southern Oscillation (ENSO) is also at play and its alignment with QBO phases can lead to large stratospheric water vapor and O_3 anomalies (Diallo et al., 2018, 2019). Here follows a hypothesis based on the results of previous studies to explain the interhemispheric asymmetry building up in long-lived tracers and AoA from 2006–2007 to 2011–2012. As in earlier studies (see e.g., Figure 13 in Ploeger & Birner, 2016, Figure 4 in Diallo et al., 2018, or Figure 3 in Strahan et al., 2020), the 2010–2011 period stands out in Figure 8 as a period of particularly strong interhemispheric difference, whether in long-lived tracer or in AoA spectrum time series. The 2009–2013 period saw peculiarities in the QBO winds, with an intense QBO easterly wind phase starting in mid-2009 and ending in mid-2010, followed by a relatively weak westerly phase (Nedoluha et al., 2015). The strong easterly phase, starting in austral winter, could have built up low F_y anomalies in the Southern Hemisphere midlatitudes due to enhanced poleward advection from the tropics (Baldwin et al., 2001; Strahan et al., 2015). As explained in Strahan et al. (2015), a transport pathway allows the QBO-generated trace gas variability to reach the poles and persist in midlatitudes through recirculation (Ploeger & Birner, 2016). Moreover, as noted by Diallo et al. (2018), the Arctic stratospheric vortex was exceptionally strong and lasted until April 2011 (Manney et al., 2011), which corresponds to a weaker wave activity (Hurwitz et al., 2011) and thus, weaker BDC in the Northern Hemisphere. The more stable poleward transport of easterly QBO phase anomalies in the Southern Hemisphere (Strahan et al., 2015) coupled to the weak BDC in the Northern Hemisphere would then explain the strong interhemispheric difference (i.e., high and low F_y values in the Northern and Southern Hemispheres, respectively) of the period 2010–2011. Detailed quantitative analysis needs to be done in the future to support or reject this hypothesis.

7. Conclusions

Using inorganic fluorine, as retrieved ($^*F_y$, see Equation 2 and Section 4.1) from ground-based FTIR solar spectra recorded at the NDACC stations of Jungfraujoch (Switzerland, 46°N) and Lauder (New Zealand, 45°S) as well as from ACE-FTS occultation measurements and simulated (F_y, see Equation 1) by BASCOE CTM driven by five modern reanalyses, we investigated the BDC variability and long-term changes over the last 30 years. The long-term trends of inorganic fluorine analyzed in this research suggest that the midlatitude lower stratosphere of the Southern Hemisphere is getting younger relative to that of the Northern Hemisphere during the first decades of the 21st century (2004–2018; Figures 6g–6i and 8). While we noted large differences between the reanalyses, we showed that all of them capture this interhemispheric asymmetry. This result, based on observations and CTM simulations driven by meteorological reanalyses, is in contrast with the CCM projections for the 21st century in response to the coupled increase of greenhouse gases and decrease of ODS (see Section 1). Indeed, CCMs simulate a much less accelerated BDC in response to the greenhouse gases increase when the forcing of the ODS decrease is taken into account, with a larger impact of the latter in the Southern Hemisphere due to the ozone hole recovery, that is, a decelerated BDC in the Southern Hemisphere (Polvani et al., 2019). These conflicting results, between observed and CCM-modeled BDC long-term trends, were also recently noted by Strahan et al. (2020) from global and multidecadal observations of HCl and HNO_3. These disagreements between observations and CCMs, also highlighted recently in Ball et al. (2020) for midlatitude ozone trends, await further investigations as these same models are used to project the health of the ozone layer as ODS decline and climate changes.

The large differences in stratospheric transport evaluated in modern reanalyses were noted in previous studies. A direct comparison between earlier AoA results (Chabrillat et al., 2018) and the present work highlights the relation between the assessed AoA of reanalyses and our F_y time series, with older AoA causing larger F_y columns in the midlatitudes. Our comparison with FTIR observations shows that the F_y trend produced by ERA-Interim above Jungfraujoch is unrealistically low for the 1990–1999 period. An important original result of this study is that ERA5, the new ECMWF reanalysis, seems more suitable than ERA-Interim to drive kinematic CTMs such as the BASCOE CTM (Figures 4–6 and 8).

While we did not investigate the cause of the BDC circulation changes, we emphasize here the importance of multidecadal time series of observations as proposed today by the FTIR NDACC network as well as by

the ACE-FTS or the Aura Microwave Limb Sounder (MLS) satellite instruments. Large disagreements or differences are indeed depicted between CCMs simulations, reanalyses, and observations (Section 1). The differences between reanalyses are not limited to the 20th century when observations were sparser and less precise (e.g., vertically resolved) than they are today. Disagreements between reanalyses can, in fact, be larger for the last two decades than for the 1990s. Moreover, seeing these large discrepancies, it seems that studies assessing trends in the last decades (e.g., estimations of the current status of ozone layer healing) should not rely on only one reanalysis and should choose the periods for the trend evaluation with care.

Besides their utility in this study, we demonstrate that the multidecadal $^*F_y$ time series of inorganic fluorine as retrieved from the ground-based FTIR stations of Lauder and Jungfraujoch are a very good approximation of the total inorganic fluorine F_y. This is important as these long-term time series is needed to scrutinize the fulfillment of the Montreal Protocol on Substances that Deplete the Ozone Layer, now that HFCs are also regulated (see Section 1).

Data Availability Statement

FTIR and model data discussed in this study are available in Prignon et al. (2021). See Bernath et al. (2020) for ACE-FTS data. ERA5 data are available at https://cds.climate.copernicus.eu/ (last access: March 26, 2021), ERA-Interim data are available at https://apps.ecmwf.int/datasets/ (last access: March 26, 2021), JRA-55 data are available at https://rda.ucar.edu/(last access: March 26, 2021) and MERRA and MERRA-2 data are available at https://disc.gsfc.nasa.gov/datasets/ (last access: March 26, 2021).

Acknowledgments
The authors are grateful to the International Foundation High Altitude Research Stations Jungfraujoch and Gornergrat (HFSJG, Bern) for supporting the facilities needed to perform the FTIR observations at Jungfraujoch. Measurements at Lauder are core-funded by NIWA (program CAAC_2101) through New Zealand's Ministry of Business, Innovation, and Employment Strategic Science Investment Fund. The Atmospheric Chemistry Experiment mission is funded by the Canadian Space Agency. The authors thank the reanalysis centers (ECMWF, NASA GSFC, and JMA) for providing their support and data products. The TOMCAT modeling work was supported by the NERC SISLAC project (NE/R001782/1) and used the national Archer and Leeds ARC HPC facilities. S. E. Strahan thanks the NASA ACMA program for support. M. Prignon and D. Minganti were financially supported by the F.R.S.—FNRS (Brussels) through the ACCROSS research project (Grant no. PDR.T.0040.16). The University of Liège contribution was further supported by the GAW-CH program of MeteoSwiss and the Fédération Wallonie-Bruxelles. E. Mahieu is a senior research associate with the F.R.S.—FNRS. The authors thank Olivier Flock for their vital contribution to the maintenance of our infrastructures and to the FTIR observations. The authors further thank Yves Christophe and Quentin Errera (BIRA-IASB, Brussels, Belgium) for their contributions to the development of BASCOE.

References

Abalos, M., Polvani, L., Calvo, N., Kinnison, D., Ploeger, F., Randel, W., & Solomon, S. (2019). New insights on the impact of ozone-depleting substances on the Brewer-Dobson circulation. *Journal of Geophysical Research: Atmospheres*, *124*(5), 2435–2451. https://doi.org/10.1029/2018JD029301

Bader, W., Bovy, B., Conway, S., Strong, K., Smale, D., Turner, A. J., et al. (2017). The recent increase of atmospheric methane from 10 years of ground-based NDACC FTIR observations since 2005. *Atmospheric Chemistry and Physics*, *17*(3), 2255–2277. https://doi.org/10.5194/acp-17-2255-2017

Baldwin, M. P., Gray, L. J., Dunkerton, T. J., Hamilton, K., Haynes, P. H., Randel, W. J., et al. (2001). The quasi-biennial oscillation. *Reviews of Geophysics*, *39*(2), 179–229. https://doi.org/10.1029/1999RG000073

Ball, W. T., Chiodo, G., Abalos, M., Alsing, J., & Stenke, A. (2020). Inconsistencies between chemistry-climate models and observed lower stratospheric ozone trends since 1998. *Atmospheric Chemistry and Physics*, *20*(16), 9737–9752. https://doi.org/10.5194/acp-20-9737-2020

Banerjee, A., Fyfe, J. C., Polvani, L. M., Waugh, D., & Chang, K. L. (2020). A pause in Southern Hemisphere circulation trends due to the Montreal Protocol. *Nature*, *579*(7800), 544–548. https://doi.org/10.1038/s41586-020-2120-4

Bernath, P. F. (2017). The atmospheric chemistry experiment (ACE). *Journal of Quantitative Spectroscopy and Radiative Transfer*, *186*, 3–16. https://doi.org/10.1016/j.jqsrt.2016.04.006

Bernath, P. F., McElroy, C. T., Abrams, M. C., Boone, C. D., Butler, M., Camy-Peyret, C., et al. (2005). Atmospheric chemistry experiment (ACE): Mission overview. *Geophysical Research Letters*, *32*(15), L15S01. https://doi.org/10.1029/2005GL022386

Bernath, P. F., Steffen, J., Crouse, J., & Boone, C. D. (2020). Sixteen-year trends in atmospheric trace gases from orbit. *Journal of Quantitative Spectroscopy and Radiative Transfer*, *253*, 107178. https://doi.org/10.1016/j.jqsrt.2020.107178

Butchart, N. (2014). The Brewer-Dobson circulation. *Reviews of Geophysics*, *52*(2), 157–184. https://doi.org/10.1002/2013RG000448

Chabrillat, S., Vigouroux, C., Christophe, Y., Engel, A., Errera, Q., Minganti, D., et al. (2018). Comparison of mean age of air in five reanalyses using the BASCOE transport model. *Atmospheric Chemistry and Physics*, *18*(19), 14715–14735. https://doi.org/10.5194/acp-18-14715-2018

Chipperfield, M. P. (2006). New version of the TOMCAT/SLIMCAT off-line chemical transport model: Intercomparison of stratospheric tracer experiments. *Quarterly Journal of the Royal Meteorological Society*, *132*(617), 1179–1203. https://doi.org/10.1256/qj.05.51

Chirkov, M., Stiller, G. P., Laeng, A., Kellmann, S., von Clarmann, T., Boone, C. D., et al. (2016). Global HCFC-22 measurements with MIPAS: Retrieval, validation, global distribution and its evolution over 2005–2012. *Atmospheric Chemistry and Physics*, *16*(5), 3345–3368. https://doi.org/10.5194/acp-16-3345-2016

De Mazière, M., Thompson, A. M., Kurylo, M. J., Wild, J. D., Bernhard, G., Blumenstock, T., et al. (2018). The Network for the Detection of Atmospheric Composition Change (NDACC): History, status and perspectives. *Atmospheric Chemistry and Physics*, *18*(7), 4935–4964. https://doi.org/10.5194/acp-18-4935-2018

Dee, D. P., Uppala, S. M., Simmons, A. J., Berrisford, P., Poli, P., Kobayashi, S., et al. (2011). The ERA-Interim reanalysis: Configuration and performance of the data assimilation system. *Quarterly Journal of the Royal Meteorological Society*, *137*(656), 553–597. https://doi.org/10.1002/qj.828

Dhomse, S. S., Chipperfield, M. P., Damadeo, R. P., Zawodny, J. M., Ball, W. T., Feng, W., et al. (2016). On the ambiguous nature of the 11 year solar cycle signal in upper stratospheric ozone. *Geophysical Research Letters*, *43*(13), 7241–7249. https://doi.org/10.1002/2016GL069958

Dhomse, S. S., Chipperfield, M. P., Feng, W., Hossaini, R., Mann, G. W., & Santee, M. L. (2015). Revisiting the hemispheric asymmetry in midlatitude ozone changes following the Mount Pinatubo eruption: A 3-D model study. *Geophysical Research Letters*, *42*(8), 3038–3047. https://doi.org/10.1002/2015GL063052

Dhomse, S. S., Feng, W., Montzka, S. A., Hossaini, R., Keeble, J., Pyle, J. A., et al. (2019). Delay in recovery of the Antarctic ozone hole from unexpected CFC-11 emissions. *Nature Communications*, *10*, 5781. https://doi.org/10.1038/s41467-019-13717-x

Diallo, M., Konopka, P., Santee, M. L., Müller, R., Tao, M., Walker, K. A., et al. (2019). Structural changes in the shallow and transition branch of the Brewer-Dobson circulation induced by El Niño. *Atmospheric Chemistry and Physics*, *19*(1), 425–446. https://doi.org/10.5194/acp-19-425-2019

Diallo, M., Riese, M., Birner, T., Konopka, P., Müller, R., Hegglin, M. I., et al. (2018). Response of stratospheric water vapor and ozone to the unusual timing of El Niño and the QBO disruption in 2015–2016. *Atmospheric Chemistry and Physics*, *18*(17), 13055–13073. https://doi.org/10.5194/acp-18-13055-2018

Duchatelet, P., Demoulin, P., Hase, F., Ruhnke, R., Feng, W., Chipperfield, M. P., et al. (2010). Hydrogen fluoride total and partial column time series above the Jungfraujoch from long-term FTIR measurements: Impact of the line-shape model, characterization of the error budget and seasonal cycle, and comparison with satellite and model data. *Journal of Geophysical Research: Atmospheres*, *115*(22), 1–20. https://doi.org/10.1029/2010JD014677

Duchatelet, P., Mahieu, E., Ruhnke, R., Feng, W., Chipperfield, M., Demoulin, P., et al. (2009). An approach to retrieve information on the carbonyl fluoride (COF_2) vertical distributions above Jungfraujoch by FTIR multi-spectrum multi-window fitting. *Atmospheric Chemistry and Physics*, *9*(22), 9027–9042. https://doi.org/10.5194/acp-9-9027-2009

Engel, A., Bönisch, H., Ullrich, M., Sitals, R., Membrive, O., Danis, F., & Crevoisier, C. (2017). Mean age of stratospheric air derived from AirCore observations. *Atmospheric Chemistry and Physics*, *17*(11), 6825–6838. https://doi.org/10.5194/acp-17-6825-2017

Engel, A., Möbius, T., Bönisch, H., Schmidt, U., Heinz, R., Levin, I., et al. (2009). Age of stratospheric air unchanged within uncertainties over the past 30 years. *Nature Geoscience*, *2*(1), 28–31. https://doi.org/10.1038/ngeo388

Errera, Q., Chabrillat, S., Christophe, Y., Debosscher, J., Hubert, D., Lahoz, W., et al. (2019). Technical note: Reanalysis of Aura MLS chemical observations. *Atmospheric Chemistry and Physics*, *19*(21), 13647–13679. https://doi.org/10.5194/acp-19-13647-2019

Eskes, H., Huijnen, V., Arola, A., Benedictow, A., Blechschmidt, A.-M., Botek, E., et al. (2015). Validation of reactive gases and aerosols in the MACC global analysis and forecast system. *Geoscientific Model Development*, *8*(11), 3523–3543. https://doi.org/10.5194/gmd-8-3523-2015

Franco, B., Bader, W., Toon, G. C., Bray, C., Perrin, A., Fischer, E. V., et al. (2015). Retrieval of ethane from ground-based FTIR solar spectra using improved spectroscopy: Recent burden increase above Jungfraujoch. *Journal of Quantitative Spectroscopy and Radiative Transfer*, *160*, 36–49. https://doi.org/10.1016/j.jqsrt.2015.03.017

Friedrich, M., Beutner, E., Reuvers, H., Smeekes, S., Urbain, J.-P., Bader, W., et al. (2020). A statistical analysis of time trends in atmospheric ethane. *Climate Change*, *162*(1), 105–125. https://doi.org/10.1007/s10584-020-02806-2

Friedrich, M., Smeekes, S., & Urbain, J. P. (2020). Autoregressive wild bootstrap inference for nonparametric trends. *Journal of Econometrics*, *214*(1), 81–109. https://doi.org/10.1016/j.jeconom.2019.05.006

Fritsch, F., Garny, H., Engel, A., Bönisch, H., & Eichinger, R. (2020). Sensitivity of age of air trends to the derivation method for non-linear increasing inert SF6. *Atmospheric Chemistry and Physics*, *20*(14), 8709–8725. https://doi.org/10.5194/acp-20-8709-2020

Fu, Q., Solomon, S., Pahlavan, H. A., & Lin, P. (2019). Observed changes in Brewer–Dobson circulation for 1980–2018. *Environmental Research Letters*, *14*(11), 114026. https://doi.org/10.1088/1748-9326/ab4de7

Fujiwara, M., Wright, J. S., Manney, G. L., Gray, L. J., Anstey, J., Birner, T., et al. (2017). Introduction to the SPARC Reanalysis Intercomparison Project (S-RIP) and overview of the reanalysis systems. *Atmospheric Chemistry and Physics Discussions*, *17*(2), 1417–1452. https://doi.org/10.5194/acp-17-1417-2017

Garcia, R. R., Randel, W. J., & Kinnison, D. E. (2011). On the determination of age of air trends from atmospheric trace species. *Journal of the Atmospheric Sciences*, *68*(1), 139–154. https://doi.org/10.1175/2010JAS3527.1

Gardiner, T., Forbes, A., de Mazière, M., Vigouroux, C., Mahieu, E., Demoulin, P., et al. (2008). Trend analysis of greenhouse gases over Europe measured by a network of ground-based remote FTIR instruments. *Atmospheric Chemistry and Physics*, *8*(22), 6719–6727. https://doi.org/10.5194/acp-8-6719-2008

Gelaro, R., McCarty, W., Suárez, M. J., Todling, R., Molod, A., Takacs, L., et al. (2017). The modern-era retrospective analysis for research and applications, version 2 (MERRA-2). *Journal of Climate*, *30*(14), 5419–5454. https://doi.org/10.1175/JCLI-D-16-0758.1

Glatthor, N., Höpfner, M., Leyser, A., Stiller, G. P., von Clarmann, T., Grabowski, U., et al. (2017). Global carbonyl sulfide (OCS) measured by MIPAS/Envisat during 2002–2012. *Atmospheric Chemistry and Physics*, *17*(4), 2631–2652. https://doi.org/10.5194/acp-17-2631-2017

Haenel, F. J., Stiller, G. P., von Clarmann, T., Funke, B., Eckert, E., Glatthor, N., et al. (2015). Reassessment of MIPAS age of air trends and variability. *Atmospheric Chemistry and Physics*, *15*(22), 13161–13176. https://doi.org/10.5194/acp-15-13161-2015

Han, Y., Tian, W., Chipperfield, M. P., Zhang, J., Wang, F., Sang, W., et al. (2019). Attribution of the hemispheric asymmetries in trends of stratospheric trace gases inferred from microwave limb sounder (MLS) measurements. *Journal of Geophysical Research: Atmospheres*, *124*(12), 6283–6293. https://doi.org/10.1029/2018JD029723

Harrison, J. J., Chipperfield, M. P., Boone, C. D., Dhomse, S. S., Bernath, P. F., Froidevaux, L., et al. (2016). Satellite observations of stratospheric hydrogen fluoride and comparisons with SLIMCAT calculations. *Atmospheric Chemistry and Physics*, *16*(16), 10501–10519. https://doi.org/10.5194/acp-16-10501-2016

Harrison, J. J., Chipperfield, M. P., Dudhia, A., Cai, S., Dhomse, S., Boone, C. D., & Bernath, P. F. (2014). Satellite observations of stratospheric carbonyl fluoride. *Atmospheric Chemistry and Physics*, *14*(21), 11915–11933. https://doi.org/10.5194/acp-14-11915-2014

Hersbach, H., Bell, B., Berrisford, P., Hirahara, S., Horányi, A., Nicolas, J., et al. (2020). The ERA5 global reanalysis. *Quarterly Journal of the Royal Meteorological Society*, *146*(730), 1999–2049. https://doi.org/10.1002/qj.3803

Huijnen, V., Flemming, J., Chabrillat, S., Errera, Q., Christophe, Y., Blechschmidt, A.-M., et al. (2016). C-IFS-CB05-BASCOE: Stratospheric chemistry in the integrated forecasting system of ECMWF. *Geoscientific Model Development*, *9*(9), 3071–3091. https://doi.org/10.5194/gmd-9-3071-2016

Hurwitz, M. M., Newman, P. A., & Garfinkel, C. I. (2011). The Arctic vortex in March 2011: A dynamical perspective. *Atmospheric Chemistry and Physics*, *11*(22), 11447–11453. https://doi.org/10.5194/acp-11-11447-2011

Kobayashi, S., Ota, Y., Harada, Y., Ebita, A., Moriya, M., Onoda, H., et al. (2015). The JRA-55 reanalysis: General specifications and basic characteristics. *Journal of the Meteorological Society of Japan Series II*, *93*(1), 5–48. https://doi.org/10.2151/jmsj.2015-001

Kohlhepp, R., Ruhnke, R., Chipperfield, M. P., De Mazière, M., Notholt, J., Barthlott, S., et al. (2012). Observed and simulated time evolution of HCl, $ClONO_2$, and HF total column abundances. *Atmospheric Chemistry and Physics*, *12*(7), 3527–3556. https://doi.org/10.5194/acp-12-3527-2012

Langerock, B., De Mazière, M., Hendrick, F., Vigouroux, C., Desmet, F., Dils, B., & Niemeijer, S. (2015). Description of algorithms for co-locating and comparing gridded model data with remote-sensing observations. *Geoscientific Model Development*, *8*(3), 911–921. https://doi.org/10.5194/gmd-8-911-2015

Lin, S.-J., & Rood, R. B. (1996). Multidimensional flux-form semi-Lagrangian transport schemes. *Monthly Weather Review*, *124*(9), 2046–2070. https://doi.org/10.1175/1520-0493(1996)124<2046:MFFSLT>2.0.CO;2

Mahieu, E., Chipperfield, M. P., Notholt, J., Reddmann, T., Anderson, J., Bernath, P. F., et al. (2014). Recent Northern Hemisphere stratospheric HCl increase due to atmospheric circulation changes. *Nature*, *515*(7525), 104–107. https://doi.org/10.1038/nature13857

Mahieu, E., Lejeune, B., Bovy, B., Servais, C., Toon, G. C., Bernath, P. F., et al. (2017). Retrieval of HCFC-142b (CH_3CClF_2) from ground-based high-resolution infrared solar spectra: Atmospheric increase since 1989 and comparison with surface and satellite measurements. *Journal of Quantitative Spectroscopy and Radiative Transfer*, *186*, 96–105. https://doi.org/10.1016/j.jqsrt.2016.03.017

Manney, G. L., Santee, M. L., Rex, M., Livesey, N. J., Pitts, M. C., Veefkind, P., et al. (2011). Unprecedented Arctic ozone loss in 2011. *Nature*, *478*(7370), 469–475. https://doi.org/10.1038/nature10556

Matthes, K., Funke, B., Andersson, M. E., Barnard, L., Beer, J., Charbonneau, P., et al. (2017). Solar forcing for CMIP6 (v3.2). *Geoscientific Model Development*, *10*(6), 2247–2302. https://doi.org/10.5194/gmd-10-2247-2017

Meinshausen, M., Nicholls, Z. R. J., Lewis, J., Gidden, M. J., Vogel, E., Freund, M., et al. (2020). The shared socio-economic pathway (SSP) greenhouse gas concentrations and their extensions to 2500. *Geoscientific Model Development*, *13*(8), 3571–3605. https://doi.org/10.5194/gmd-13-3571-2020

Meinshausen, M., Vogel, E., Nauels, A., Lorbacher, K., Meinshausen, N., Etheridge, D. M., et al. (2017). Historical greenhouse gas concentrations for climate modelling (CMIP6). *Geoscientific Model Development*, *10*(5), 2057–2116. https://doi.org/10.5194/gmd-10-2057-2017

Melen, F., Mahieu, E., Zander, R., Rinsland, C. P., Demoulin, P., Roland, G., et al. (1998). Vertical column abundances of COF_2 above the Jungfraujoch Station, derived from ground-based infrared solar observations. *Journal of Atmospheric Chemistry*, *29*(2), 119–134. https://doi.org/10.1023/A:1005847829686

Ménard, R., Chabrillat, S., Robichaud, A., de Grandpré, J., Charron, M., Rochon, Y., et al. (2020). Coupled stratospheric chemistry-meteorology data assimilation. Part I: Physical background and coupled modeling aspects. *Atmosphere*, *11*(2), 1–39. https://doi.org/10.3390/atmos11020150

Nassar, R., Bernath, P. F., Boone, C. D., McLeod, S. D., Skelton, R., Walker, K. A., et al. (2006). A global inventory of stratospheric fluorine in 2004 based on Atmospheric Chemistry Experiment Fourier transform spectrometer (ACE-FTS) measurements. *Journal of Geophysical Research*, *111*(22), 1–10. https://doi.org/10.1029/2006JD007395

Nedoluha, G. E., Boyd, I. S., Parrish, A., Gomez, R. M., Allen, D. R., Froidevaux, L., et al. (2015). Unusual stratospheric ozone anomalies observed in 22 years of measurements from Lauder, New Zealand. *Atmospheric Chemistry and Physics*, *15*(12), 6817–6826. https://doi.org/10.5194/acp-15-6817-2015

Notholt, J., & Lehmann, R. (2003). The moon as light source for atmospheric trace gas observations: Measurement technique and analysis method. *Journal of Quantitative Spectroscopy and Radiative Transfer*, *76*(3–4), 435–445. https://doi.org/10.1016/S0022-4073(02)00069-9

Osprey, S. M., Butchart, N., Knight, J. R., Scaife, A. A., Hamilton, K., Anstey, J. A., et al. (2016). An unexpected disruption of the atmospheric quasi-biennial oscillation. *Science*, *353*(6306), 1424–1427. https://doi.org/10.1126/science.aah4156

Ploeger, F., Abalos, M., Birner, T., Konopka, P., Legras, B., Müller, R., & Riese, M. (2015). Quantifying the effects of mixing and residual circulation on trends of stratospheric mean age of air. *Geophysical Research Letters*, *42*(6), 2047–2054. https://doi.org/10.1002/2014GL062927

Ploeger, F., & Birner, T. (2016). Seasonal and inter-annual variability of lower stratospheric age of air spectra. *Atmospheric Chemistry and Physics*, *16*(15), 10195–10213. https://doi.org/10.5194/acp-16-10195-2016

Ploeger, F., Legras, B., Charlesworth, E., Yan, X., Diallo, M., Konopka, P., et al. (2019). How robust are stratospheric age of air trends from different reanalyses? *Atmospheric Chemistry and Physics*, *19*(9), 6085–6105. https://doi.org/10.5194/acp-19-6085-2019

Plumb, R. A. (2007). Tracer interrelationships in the stratosphere. *Reviews of Geophysics*, *45*(4), 1–33. https://doi.org/10.1029/2005RG000179

Polvani, L. M., Abalos, M., Garcia, R., Kinnison, D., & Randel, W. J. (2018). Significant weakening of Brewer-Dobson circulation trends over the 21st century as a consequence of the Montreal Protocol. *Geophysical Research Letters*, *45*(1), 401–409. https://doi.org/10.1002/2017GL075345

Polvani, L. M., Wang, L., Abalos, M., Butchart, N., Chipperfield, M. P., Dameris, M., et al. (2019). Large impacts, past and future, of ozone-depleting substances on Brewer-Dobson circulation trends: A multi-model assessment. *Journal of Geophysical Research: Atmospheres*, *124*(13), 6669–6680. https://doi.org/10.1029/2018JD029516

Polvani, L. M., Wang, L., Aquila, V., & Waugh, D. W. (2017). The impact of ozone-depleting substances on tropical upwelling, as revealed by the absence of lower-stratospheric cooling since the late 1990s. *Journal of Climate*, *30*(7), 2523–2534. https://doi.org/10.1175/JCLI-D-16-0532.1

Prignon, M., Chabrillat, S., Minganti, D., O'Doherty, S., Servais, C., Stiller, G., et al. (2019). Improved FTIR retrieval strategy for HCFC-22 ($CHClF_2$), comparisons with in situ and satellite datasets with the support of models, and determination of its long-term trend above Jungfraujoch. *Atmospheric Chemistry and Physics*, *19*(19), 12309–12324. https://doi.org/10.5194/acp-19-12309-2019

Prignon, M., Chabrillat, S., Smale, D., Chipperfield, M. P., Servais, C., & Mahieu, E. (2021). *Stratospheric inorganic fluorine data from ground-based FTIR, BASCOE CTM and TOMCAT [Data set]*. Zenodo.

Ray, E. A., Portmann, R. W., Yu, P., Daniel, J., Montzka, S. A., Dutton, G. S., et al. (2020). The influence of the stratospheric Quasi-Biennial Oscillation on trace gas levels at the Earth's surface. *Nature Geoscience*, *13*(1), 22–27. https://doi.org/10.1038/s41561-019-0507-3

Rienecker, M. M., Suarez, M. J., Gelaro, R., Todling, R., Bacmeister, J., Liu, E., et al. (2011). MERRA: NASA's modern-era retrospective analysis for research and applications. *Journal of Climate*, *24*(14), 3624–3648. https://doi.org/10.1175/JCLI-D-11-00015.1

Rodgers, C. D. (2000). *Inverse methods for atmospheric sounding*. World Scientific.

Rothman, L. S., Gordon, I. E., Barbe, A., Benner, D. C., Bernath, P. F., Birk, M., et al. (2009). The HITRAN 2008 molecular spectroscopic database. *Journal of Quantitative Spectroscopy and Radiative Transfer*, *110*(9–10), 533–572. https://doi.org/10.1016/j.jqsrt.2009.02.013

Rotman, D. A., Tannahill, J. R., Kinnison, D. E., Connell, P. S., Bergmann, D., Proctor, D., et al. (2001). Global Modeling Initiative assessment model: Model description, integration, and testing of the transport shell. *Journal of Geophysical Research*, *106*(D2), 1669–1691. https://doi.org/10.1029/2000JD900463

Santer, B. D., Wigley, T. M. L., Boyle, J. S., Gaffen, D. J., Hnilo, J. J., Nychka, D., et al. (2000). Statistical significance of trends and trend differences in layer-average atmospheric temperature time series. *Journal of Geophysical Research*, *105*(D6), 7337–7356. https://doi.org/10.1029/1999JD901105

Sheese, P. E., Boone, C. D., & Walker, K. A. (2015). Detecting physically unrealistic outliers in ACE-FTS atmospheric measurements. *Atmospheric Measurement Techniques*, *8*(2), 741–750. https://doi.org/10.5194/amt-8-741-2015

Skachko, S., Ménard, R., Errera, Q., Christophe, Y., & Chabrillat, S. (2016). EnKF and 4D-Var data assimilation with chemical transport model BASCOE (version 05.06). *Geoscientific Model Development*, *9*(8), 2893–2908. https://doi.org/10.5194/gmd-9-2893-2016

Smeekes, S., & Urbain, J.-P. (2014). *A multivariate invariance principle for modified wild bootstrap methods with an application to unit root testing*. Maastricht University, Graduate School of Business and Economics. https://doi.org/10.26481/umagsb.2014008

SPARC/IO3C/GAW. (2019). *SPARC/IO3C/GAW report on long-term ozone trends and uncertainties in the stratosphere, SPARC report*.

Steffen, J., Bernath, P. F., & Boone, C. D. (2019). Trends in halogen-containing molecules measured by the Atmospheric Chemistry Experiment (ACE) satellite. *Journal of Quantitative Spectroscopy and Radiative Transfer*, *238*, 106619. https://doi.org/10.1016/j.jqsrt.2019.106619

Stiller, G. P., Fierli, F., Ploeger, F., Cagnazzo, C., Funke, B., Haenel, F. J., et al. (2017). Shift of subtropical transport barriers explains observed hemispheric asymmetry of decadal trends of age of air. *Atmospheric Chemistry and Physics*, *17*(18), 11177–11192. https://doi.org/10.5194/acp-17-11177-2017

Stiller, G. P., Von Clarmann, T., Haenel, F., Funke, B., Glatthor, N., Grabowski, U., et al. (2012). Observed temporal evolution of global mean age of stratospheric air for the 2002 to 2010 period. *Atmospheric Chemistry and Physics*, *12*(7), 3311–3331. https://doi.org/10.5194/acp-12-3311-2012

Strahan, S. E., Douglass, A. R., Newman, P. A., & Steenrod, S. D. (2014). Inorganic chlorine variability in the Antarctic vortex and implications for ozone recovery. *Journal of Geophysical Research: Atmospheres*, *119*(24), 14,098–14,109. https://doi.org/10.1002/2014JD022295

Strahan, S. E., Oman, L. D., Douglass, A. R., & Coy, L. (2015). Modulation of Antarctic vortex composition by the quasi-biennial oscillation. *Geophysical Research Letters*, *42*(10), 4216–4223. https://doi.org/10.1002/2015GL063759

Strahan, S. E., Smale, D., Douglass, A. R., Blumenstock, T., Hannigan, J. W., Hase, F., et al. (2020). Observed hemispheric asymmetry in stratospheric transport trends from 1994 to 2018. *Geophysical Research Letters*, *47*(17), 1–9. https://doi.org/10.1029/2020GL088567

Tweedy, O. V., Kramarova, N. A., Strahan, S. E., Newman, P. A., Coy, L., Randel, W. J., et al. (2017). Response of trace gases to the disrupted 2015–2016 quasi-biennial oscillation. *Atmospheric Chemistry and Physics*, *17*(11), 6813–6823. https://doi.org/10.5194/acp-17-6813-2017

Vigouroux, C., Augusto Bauer Aquino, C., Bauwens, M., Becker, C., Blumenstock, T., De Mazière, M., et al. (2018). NDACC harmonized formaldehyde time series from 21 FTIR stations covering a wide range of column abundances. *Atmospheric Measurement Techniques*, *11*(9), 5049–5073. https://doi.org/10.5194/amt-11-5049-2018

Waugh, D. W., & Hall, T. M. (2002). Age of stratospheric air: Theory, observations, and models. *Reviews of Geophysics*, *40*(4), 1-1–1–10. https://doi.org/10.1029/2000RG000101

WMO (World Meteorological Organization). (2018). *Scientific assessment of ozone depletion: 2018. Global ozone research and monitoring project (Report No. 58)*.

Zander, R., Gunson, M. R., Farmer, C. B., Rinsland, C. P., Irion, F. W., & Mahieu, E. (1992). The 1985 chlorine and fluorine inventories in the stratosphere based on ATMOS observations at 30° north latitude. *Journal of Atmospheric Chemistry*, *15*(2), 171–186. https://doi.org/10.1007/BF00053758

Zander, R., Mahieu, E., Demoulin, P., Duchatelet, P., Roland, G., Servais, C., et al. (2008). Our changing atmosphere: Evidence based on long-term infrared solar observations at the Jungfraujoch since 1950. *The Science of the Total Environment*, *391*(2–3), 184–195. https://doi.org/10.1016/j.scitotenv.2007.10.018

Zhou, M., Langerock, B., Vigouroux, C., Wang, P., Hermans, C., Stiller, G., et al. (2018). Ground-based FTIR retrievals of SF6 on Reunion Island. *Atmospheric Measurement Techniques*, *11*(2), 654–662. https://doi.org/10.5194/amt-11-651-2018